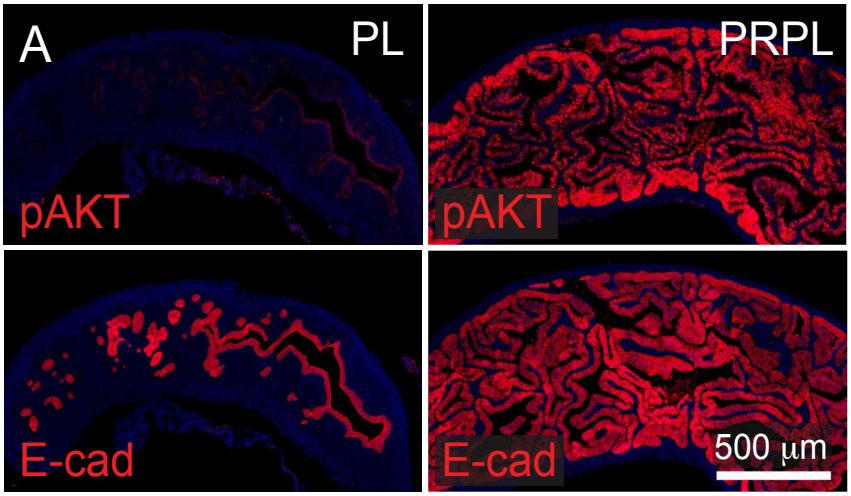

B Lymphoid gating

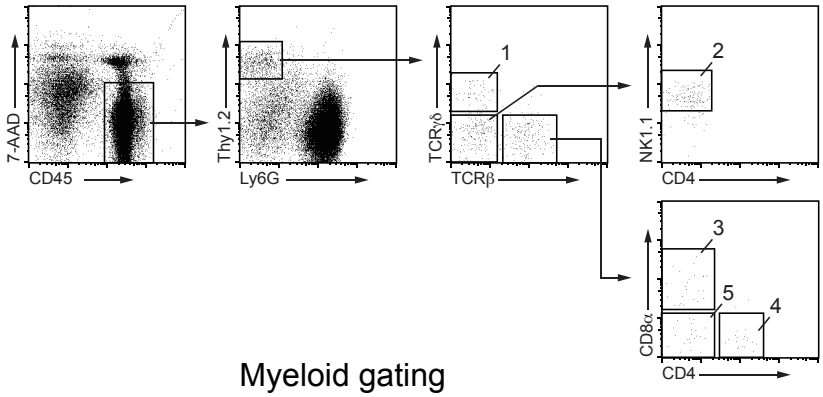

1. γδ T cells
2. NK cells
3. CD8 T cells
4. CD4 T cells
5. CD4^{-}CD8^{-} T cells

Myeloid gating

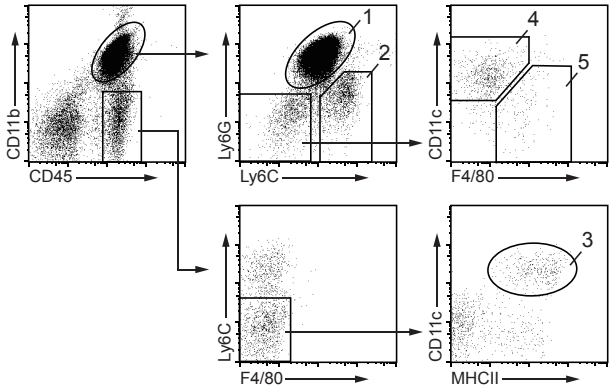

1. PMNs
2. Ly6C^{hi} monocytes
3. CD11b^{lo} DCs
4. CD11b^{hi} DCs
5. Macrophages

C

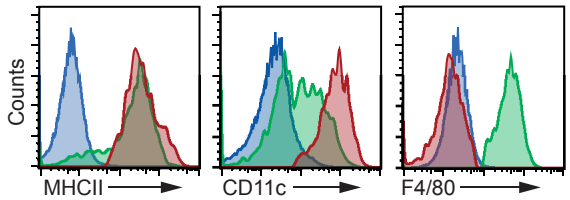

PMNs

DCs (groups 3 and 4 of myeloid gating above)

Macrophages (group 5 of myeloid gating above)

D

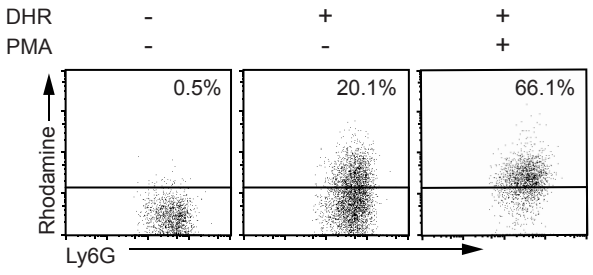
DHR - + +
PMA - - +
0.5%
20.1%
66.1%
Rhodamine
Ly6G

E

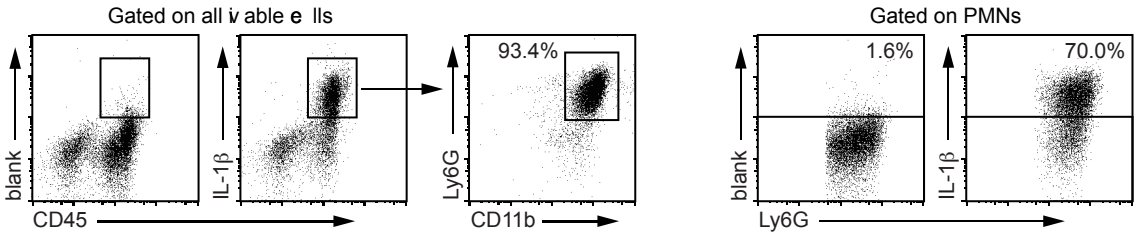
Gated on all viable cells
blank
CD45
IL-1β
93.4%
Ly6G
CD11b
Gated on PMNs
1.6%
blank
Ly6G
70.0%
IL-1β

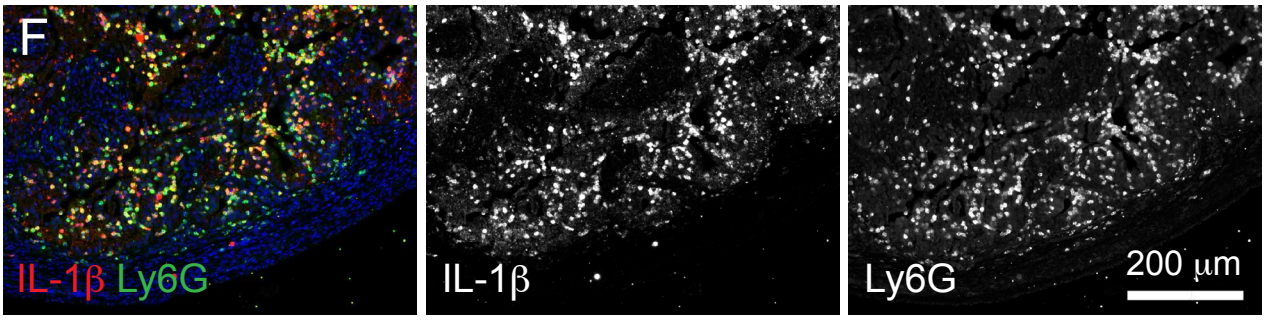
F
IL-1β Ly6G
IL-1β
Ly6G
200 μm

Figure S1, related to Figure 1. Identification and characteristics of infiltrating PMNs in early stage PRPL uteri. (A) PTEN inactivation throughout the PRPL uterine epithelium. Serial tissue sections of 2-week PL and PRPL uteri were stained with antibodies to phospho-AKT (pAKT; top) to identify cells with PTEN loss, or to E-cadherin (E-Cad; bottom) to visualize all uterine epithelial cells. Representative of n = 3 mice per group. (B) Gating strategies to identify uterine leukocyte subsets. The myeloid gating also involved use of 7-AAD to identify viable cells (not depicted). (C) Flow cytometric characteristics of uterine PMNs in comparison to uterine DCs and macrophages. (D) Reactive oxygen species (ROS) production by uterine PMNs. 4-week PRPL uterine cells were incubated for 30 min with or without dihydrorhodamine 123 (DHR), which in the presence of ROS becomes oxidized to the fluorescent compound rhodamine. Cells incubated with phorbol myristate acetate (PMA) served as a positive control for ROS production. Gated on $CD45^{+}7\text{-}AAD^{-}CD11b^{+}Ly6G^{+}$ cells as in panel B. Representative of n = 5 mice. (E) IL-1β production by uterine leukocytes, as detected by intracellular cytokine staining of uterine cell suspensions. Note that virtually all IL-$1\beta^{+}$ cells within the total viable ($7\text{-}AAD^{-}$) population are $CD45^{+}CD11b^{+}Ly6G^{+}$ PMNs (left) and that a large fraction of PMNs produce IL-1β (right). Representative of n = 5 mice. (F) Representative co-immunostaining of $Ly6G^{+}$ PMNs and IL-1β in 4-week PRPL uteri. Middle and right images show individual stains from the left panel. Most IL-$1\beta^{+}$ cells are PMNs (i.e. $Ly6G^{+}$ cells), though not all PMNs express IL-1β, consistent with the intracellular cytokine staining in panel E. Representative of n = 3 mice.

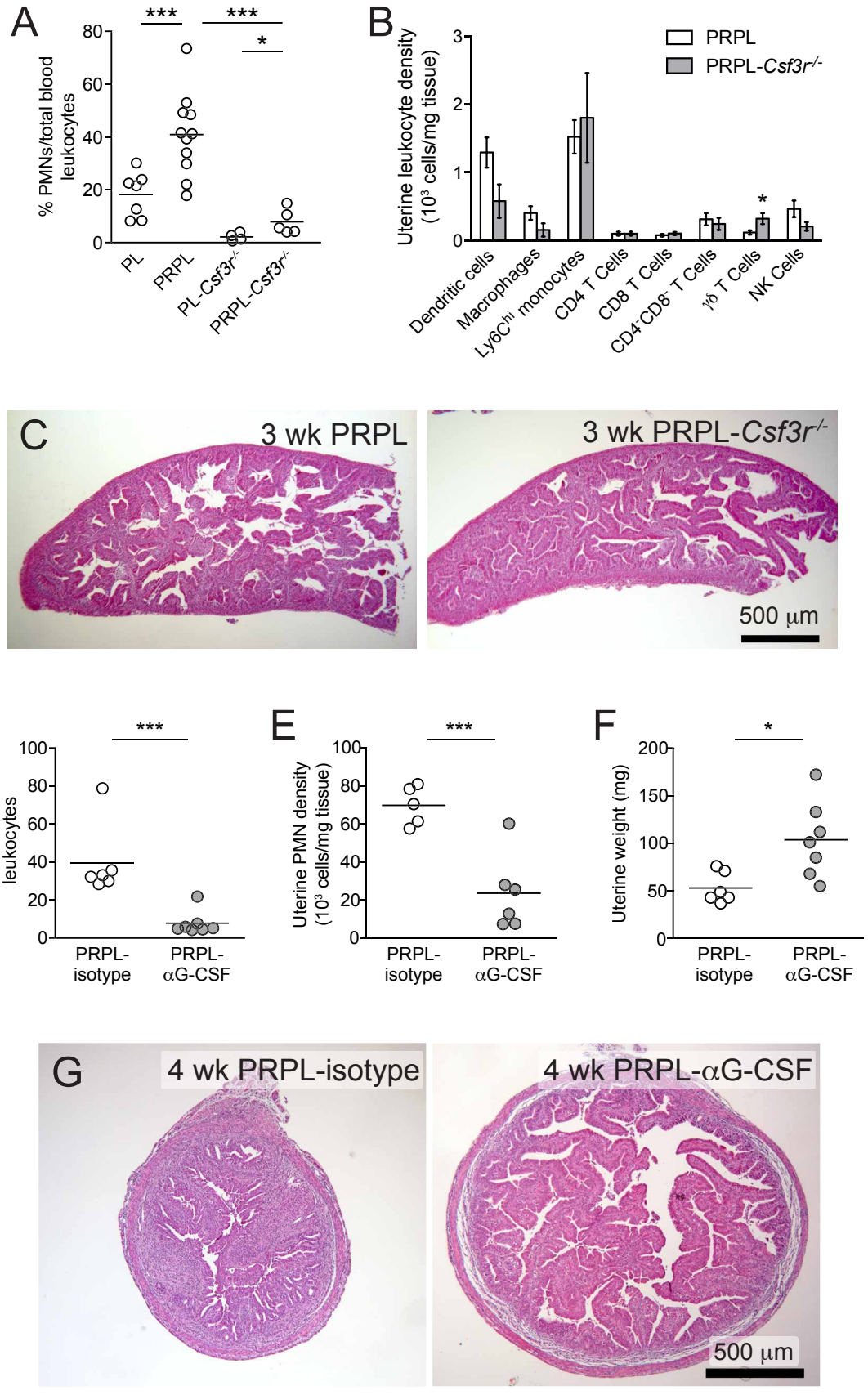
A
% PMNs/total blood leukocytes
***
***
*
PL
PRPL
PL-Csf3r-/-
PRPL-Csf3r-/-
B
Uterine leukocyte density (10³ cells/mg tissue)
PRPL
PRPL-Csf3r-/-
*
Dendritic cells
Macrophages
Ly6Chi monocytes
CD4 T Cells
CD8 T Cells
CD4-CD8- T Cells
γδ T Cells
NK Cells
C
3 wk PRPL
3 wk PRPL-Csf3r-/-
500 μm
D
% PMNs/total blood leukocytes
***
PRPL-isotype
PRPL-αG-CSF
E
Uterine PMN density (10³ cells/mg tissue)
***
PRPL-isotype
PRPL-αG-CSF
F
Uterine weight (mg)
*
PRPL-isotype
PRPL-αG-CSF
G
4 wk PRPL-isotype
4 wk PRPL-αG-CSF
500 μm

Figure S2, related to Figure 2. Further characterization of PMN-depleted tumor-bearing uteri. (A) PMN frequencies in the blood of 4-week-old mice. (B) Leukocyte subset densities in 4-week PRPL versus PRPL-*Csf3r*$^{-/-}$ uteri as determined by flow cytometry. Data show mean ± SEM for n ≥ 7 mice per group. (C) Representative H&E stained longitudinal sections from 3-week uteri (n ≥ 6 mice per group). (D-G) Effect of antibody-mediated PMN depletion on blood PMN frequencies (D), uterine PMN densities (E), uterine weights (F), and uterine morphology (G; H&E staining). PMNs were depleted in PRPL mice by giving daily injections of G-CSF-neutralizing antibodies (PRPL-αG-CSF) from postnatal day 19 until sacrifice on day 28 while control mice were similarly treated with an isotype-matched antibody (PRPL-isotype). One of the mice with the most substantial depletion of PMNs provided the image shown in panel G. *$p < 0.05$; ***$p < 0.005$.

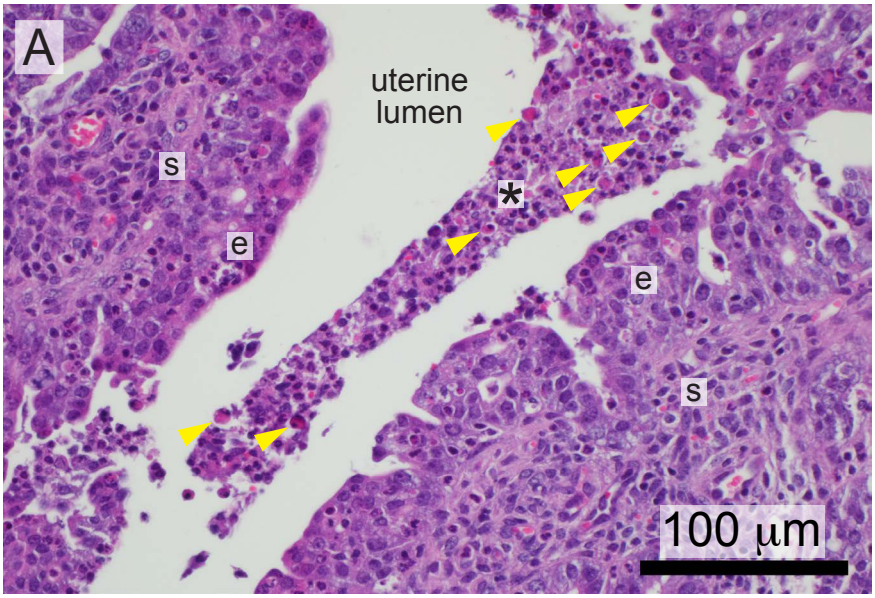
A
uterine lumen
s
e
*
e
s
100 μm

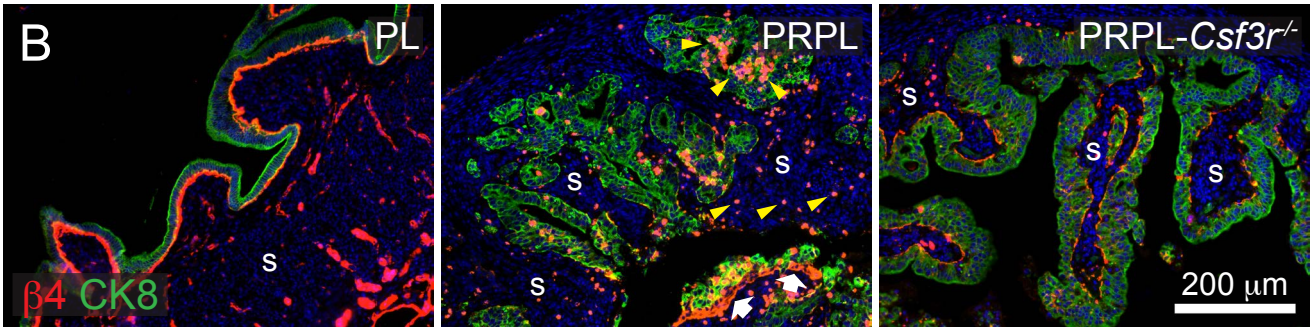
B
PL
PRPL
PRPL-Csf3r-/-
β4 CK8
s
200 μm

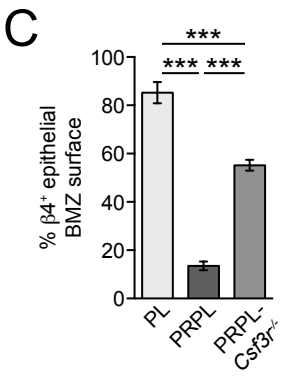
C
% β4+ epithelial BMZ surface
***
***
***
PL
PRPL
PRPL-Csf3r-/-

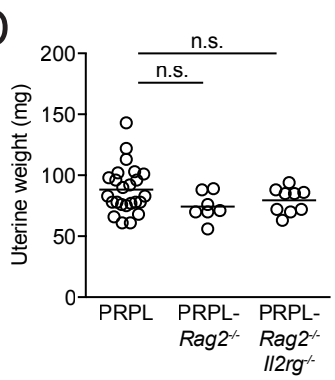
D
Uterine weight (mg)
n.s.
n.s.
PRPL
PRPL-Rag2-/-
PRPL-Rag2-/-Il2rg-/-

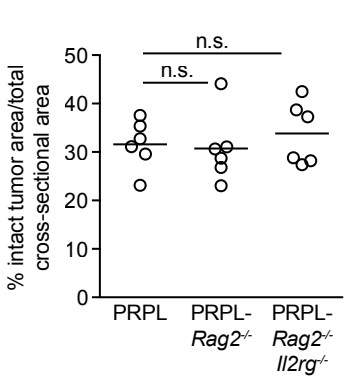
E
% intact tumor area/total cross-sectional area
n.s.
n.s.
PRPL
PRPL-Rag2-/-
PRPL-Rag2-/-Il2rg-/-

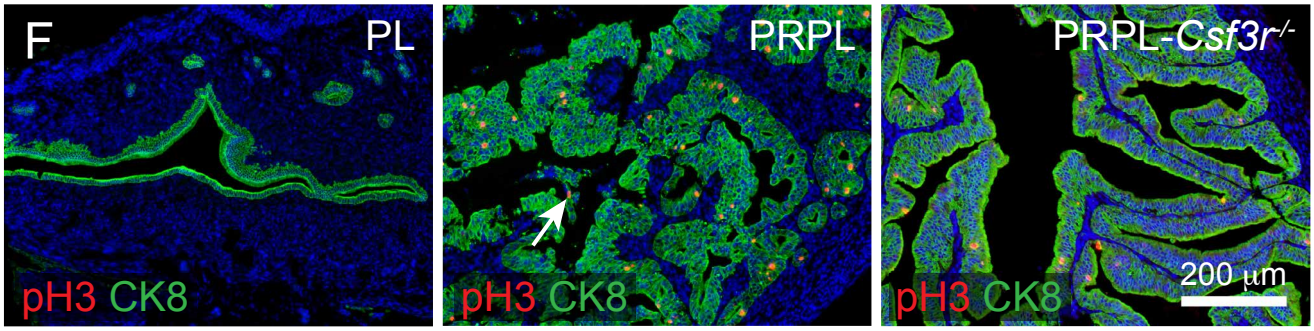
F
PL
PRPL
PRPL-Csf3r-/-
pH3 CK8
pH3 CK8
pH3 CK8
200 μm

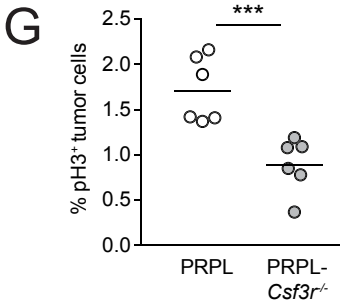
G
***
% pH3+ tumor cells
2.5
2.0
1.5
1.0
0.5
0.0
PRPL
PRPL-Csf3r-/-

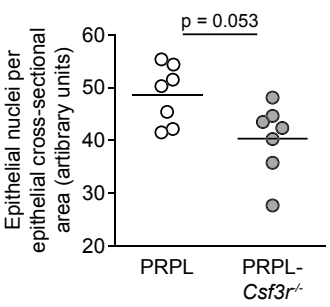
H
p = 0.053
Epithelial nuclei per epithelial cross-sectional area (aritbrary units)
60
50
40
30
20
PRPL
PRPL-Csf3r-/-

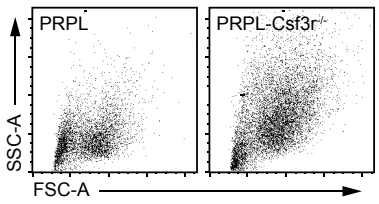
I
PRPL
PRPL-Csf3r-/-
SSC-A
FSC-A

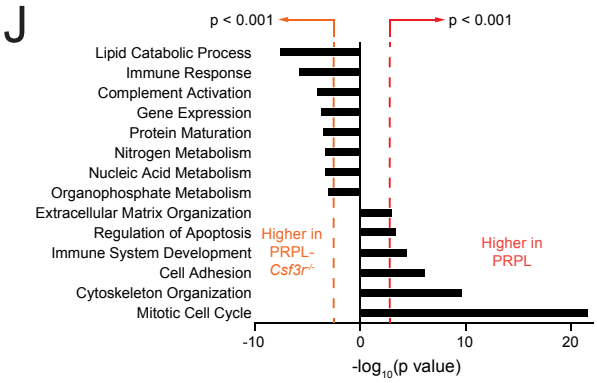
J
p < 0.001
p < 0.001
Lipid Catabolic Process
Immune Response
Complement Activation
Gene Expression
Protein Maturation
Nitrogen Metabolism
Nucleic Acid Metabolism
Organophosphate Metabolism
Extracellular Matrix Organization
Regulation of Apoptosis
Immune System Development
Cell Adhesion
Cytoskeleton Organization
Mitotic Cell Cycle
Higher in PRPL-Csf3r-/-
Higher in PRPL
-10
0
10
20
-log10(p value)

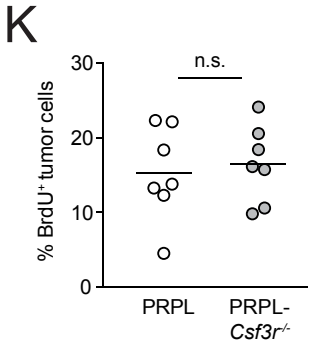
K
n.s.
% BrdU+ tumor cells
30
20
10
0
PRPL
PRPL-Csf3r-/-

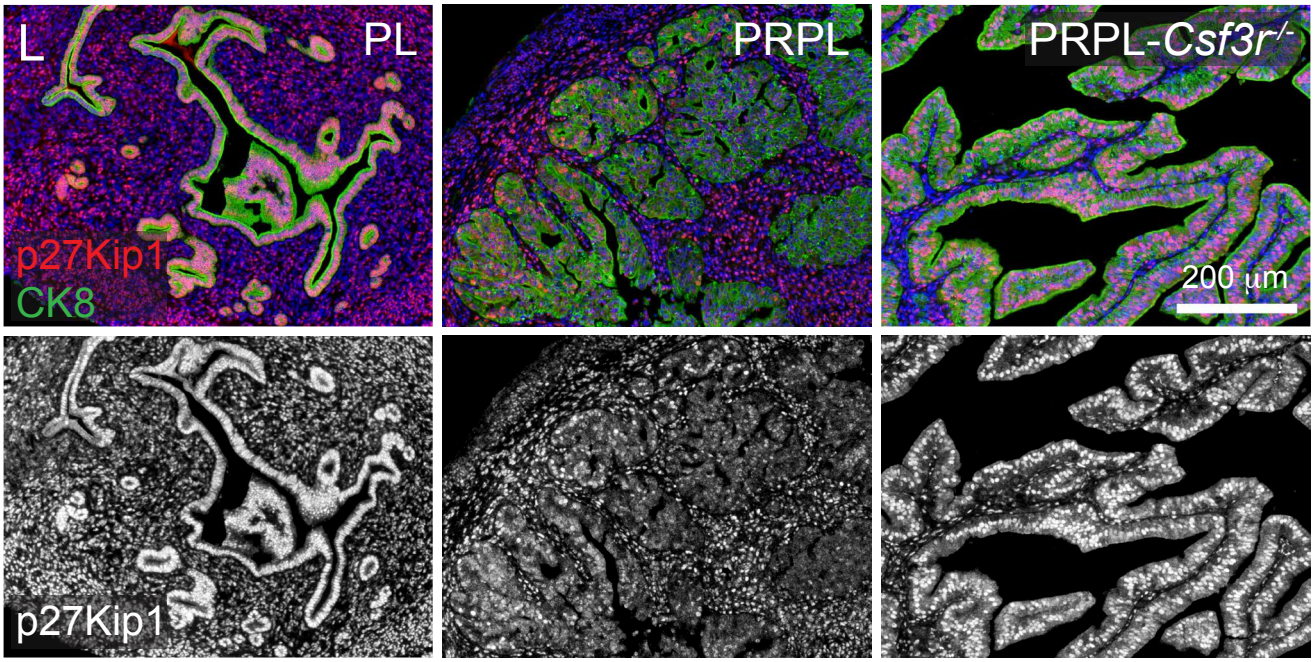
L
PL
PRPL
PRPL-Csf3r-/-
p27Kip1
CK8
200 μm
p27Kip1

M

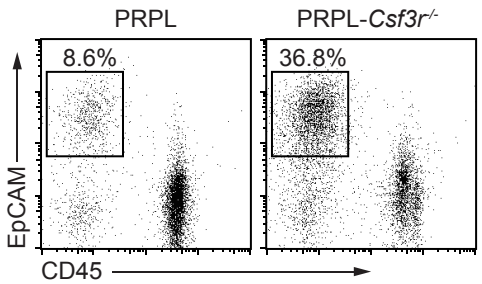

N

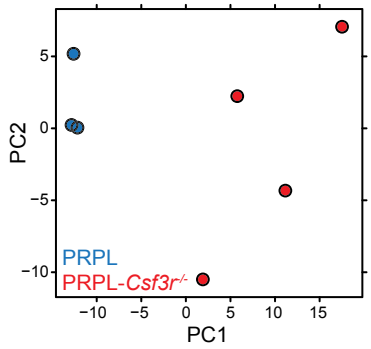

O

Gene	Gene Name	Fold	p-value
Ahctf1	AT hook containing transcription factor 1	1.20	1.66E-02
Anln	Anillin, actin binding protein	1.80	4.86E-04
Aspm	Abnormal spindle-like, microcephaly associated (*Drosophila*)	1.76	2.42E-04
Bub1	Budding uninhibited by benzimidazoles 1 homolog (*S. cerveisiae*)	1.45	1.46E-03
Bub1b	Budding uninhibited by benzimidazoles 1 homolog, beta (*S. cerveisiae*)	1.33	3.62E-02
Ccna2	Cyclin A2	1.39	1.61E-02
Ccnb1	Cyclin B1	1.55	4.87E-05
Ccnb2	Cyclin B2	1.25	4.99E-02
Ccnd1	Cyclin D1	1.48	1.48E-02
Cdc25c	Cell division cycle 25 homolog C (*S. pombe*)	1.37	3.74E-02
Cdca8	Cell division cycle associated 8	1.28	4.05E-02
Cdk6	Cyclin-dependent kinase 6	1.54	3.50E-02
Cdkn2a	Cyclin-dependent kinase inhibitor 2A	1.69	4.03E-02
Cenpe	Centromere protein E	1.46	7.50E-03
Cep55	Centrosomal protein 55	1.48	1.38E-02
Cit	Citron	1.35	4.80E-02
Ckap5	Cytoskeleton associated protein 5	1.38	8.09E-03
Cks1b	CDC28 protein kinase 1b	1.25	3.87E-02
Ercc6l	Excision repair cross-complementing rodent repair deficiency complementation group 6-like	1.50	5.88E-04
Kif11	Kinesin family member 11	1.65	4.18E-04
Kif20b	Kinesin family member 20B	1.42	1.36E-02
Kntc1	Kinetochore associated 1	1.36	3.76E-02
Lig1	Ligase I, DNA, ATP-dependent	1.22	4.33E-02
Ncapd2	Non-SMC condensin I complex, subunit D2	1.32	1.42E-02
Ncapg2	Non-SMC condensin II complex, subunit G2	1.44	1.38E-02
Ncaph	Non-SMC condensin I complex, subunit H	1.50	1.67E-03
Ndc80	NDC80 homolog, kinetochore complex component (*S. cerevisiae*)	1.42	2.73E-02
Nedd1	Neural precursor cell expressed, developmentally down-regulated gene 1	1.35	8.95E-03
Nek2	Never in mitosis gene a-related expressed kinase 2	1.38	1.93E-02
Nsl1	NSL1, MIND kinetochore complex component, homolog (*S. cerevisiae*)	1.42	3.46E-02
Nuf2	NUF2, NDC80 kinetochore complex component, homolog (*S. cerevisiae*)	1.49	3.02E-04
Nup37	Nucleoporin 37	1.32	4.26E-02
Nusap1	Nucleolar and spindle associated protein 1	1.60	2.16E-03
Pard3	Partitioning defective 3 homolog (*C. elegans*)	1.32	5.35E-03
Prc1	Protein regulator of cytokinesis 1	1.53	3.11E-03
Racgap1	Rac GTPase-activating protein 1	1.31	2.00E-02
Rad21	RAD21 homolog (*S. pombe*)	1.21	3.32E-02
Sept11	Septin 11	1.35	4.77E-02
Sept7	Septin 7	1.16	3.07E-02
Sgol1	Shugoshin-like 1 (*S. pombe*)	1.40	2.55E-02
Sgol2	Shugoshin-like 2 (*S. pombe*)	1.32	2.36E-02
Ska1	Spindle and kinetochore associated complex subunit 1	1.51	1.14E-02
Smc1a	Structural maintenance of chromosomes 1A	1.17	2.24E-02
Smc2	Structural maintenance of chromosomes 2	1.50	2.17E-03
Smc4	Structural maintenance of chromosomes 4	1.37	8.26E-03
Spag5	Sperm associated antigen 5	1.39	7.78E-03
Stag1	Stromal antigen 1	1.27	1.07E-02
Tgfb2	Transforming growth factor, beta 2	2.05	6.73E-06
Top2a	Topoisomerase (DNA) II alpha	1.50	2.63E-03
Ube2c	Ubiquitin-conjugating enzyme E2C	1.59	4.11E-04
Zwilch	Zwilch kinetochore protein	1.31	4.42E-02

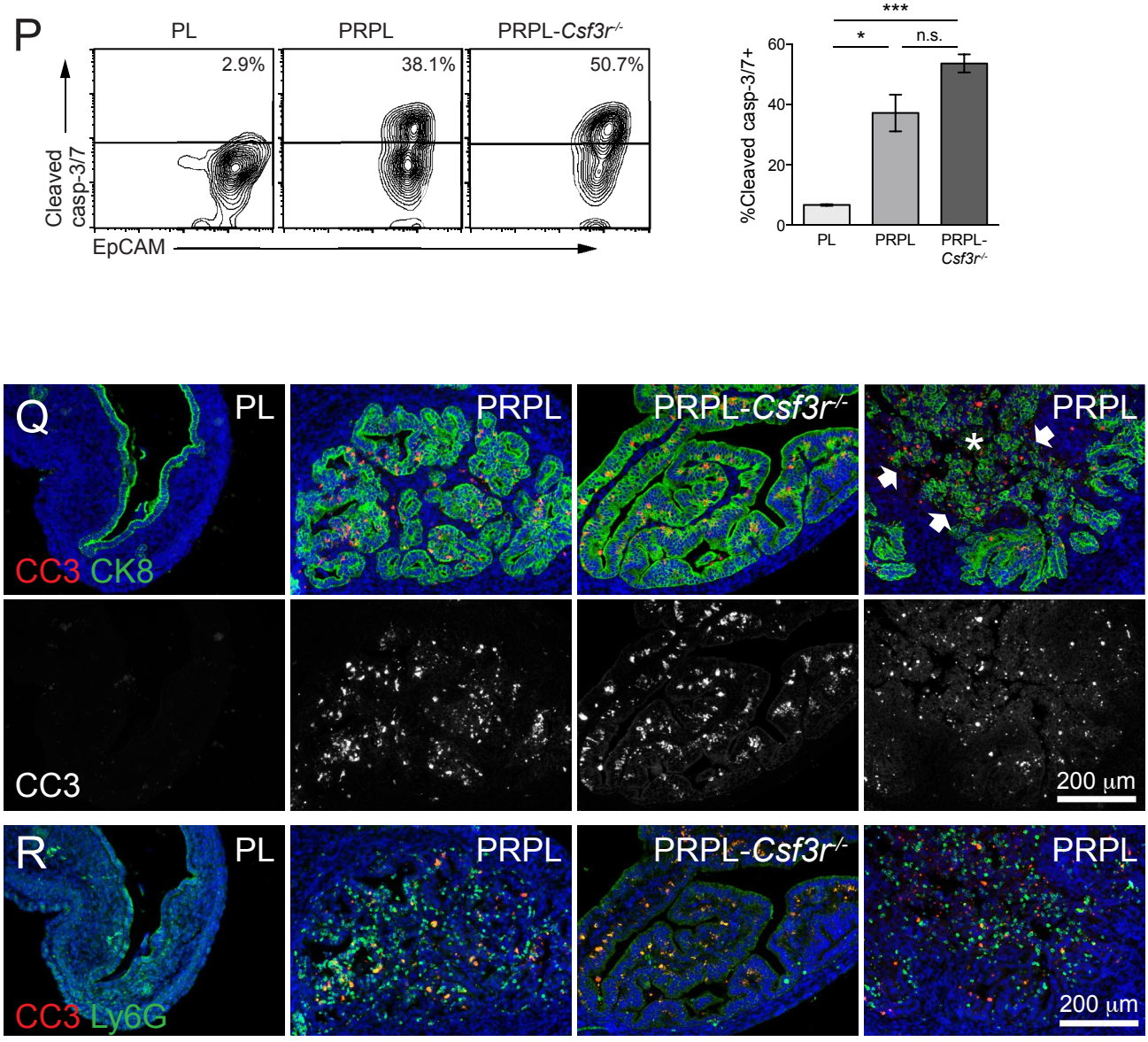
P
PL
PRPL
PRPL-Csf3r-/-
2.9%
38.1%
50.7%
Cleaved casp-3/7
EpCAM
***
*
n.s.
%Cleaved casp-3/7+
60
40
20
0
PL
PRPL
PRPL-Csf3r-/-
Q
PL
PRPL
PRPL-Csf3r-/-
PRPL
CC3 CK8
CC3
200 μm
R
PL
PRPL
PRPL-Csf3r-/-
PRPL
CC3 Ly6G
200 μm

Figure S3, related to Figure 3. Pathways of PMN-mediated tumor debulking. (A) Wide field H&E stained image of intraluminal debris in a 4-week PRPL uterus. Yellow arrowheads indicate several tumor cells with pyknotic nuclei and deeply eosinophilic cytoplasm, both indicators of early necrosis. The sharp borders of the debris in this image are likely due to it aggregating and being "molded" by the lining of the intact uterus. Asterisk: intraluminal debris; e: intact epithelium; s, stroma. (B, C) Representative images and quantified fraction of integrin β4 immunostaining in the uterine epithelial BMZ. The β4 antibody also stained PMNs (yellow arrowheads), a presumed cross-reaction given that uterine PMNs do not express this integrin subunit by flow cytometry (data not shown). The white arrows point to a stretch of BMZ in the PRPL image that shows intense β4 concentration; note the low level of staining elsewhere in this image. (D, E) Uterine weight and percent uterine cross-sectional area comprised of intact tumor epithelium in 4-week-old PRPL, PRPL-*Rag2*$^{-/-}$, and PRPL-*Rag2*$^{-/-}$*Il2rg*$^{-/-}$ mice. Tumor burden (Figure 3J) was calculated as the product of these two parameters since the latter represents the proportion of the entire uterus occupied by living tumor. PRPL data are the same as in Figure 2. (F, G) Tumor cell proliferation as assessed by pH3 immunostaining. (F) Representative 4-week tissue sections co-stained for pH3 and cytokeratin 8 (CK8) and (G) quantification of tumor cell positivity for pH3 within the intact CK8$^+$ tumor epithelium (***$p < 0.005$), demonstrating that 4-week PRPL tumor cells are proliferating more rapidly than 4-week PRPL-*Csf3r*$^{-/-}$ tumor cells. White arrow: pH3$^+$ tumor cell within intraluminal debris. Consistent with more rapid cycling, PRPL tumor cells were also smaller than their 4-week PRPL-*Csf3r*$^{-/-}$ counterparts as evidenced by (H) increased epithelial cell density, which was determined histologically as the number of epithelial nuclei per unit area of intact, CK8$^+$ tumor epithelium (see Supplemental Experimental Procedures) and (I) a flow cytometric analysis of viable tumor cells in 4-week uterine cell suspensions (representative of n = 4 mice per group). Viable tumor cells were gated as 7-AAD$^-$CD45$^-$EpCAM$^+$, as in panel M. More rapid PRPL tumor cell cycling was also indicated by functional annotation of transcripts with significantly ($p_{adj} < 0.05$) altered expression in RNA-seq data from 4-week sorted tumor cells (J), which revealed that genes associated with cell cycling were by far the most significantly enriched group in PRPL versus PRPL-*Csf3r*$^{-/-}$ sorted tumor cells. The panel shows gene ontology (GO) terms with the highest ($p < 0.001$) levels of significance (n = 3-4 samples per group). See also panels M-O below. (K) Notably, *in vivo* detection of cells in S phase via BrdU incorporation revealed comparable levels of BrdU$^+$ tumor cells within the intact, CK8$^+$ tumor epithelium of 4-week-old PRPL and PRPL-*Csf3r*$^{-/-}$ mice. BrdU was injected 2 hr prior to sacrifice. The discrepancy between pH3 and BrdU labeling presumably reflects proportionally shorter lengths of multiple phases of the cell cycle (aside from M phase) in PRPL tumor cells (Nowakowski et al., 1989). (L) As one potential mechanism of increased cycling, PRPL but not PRPL-*Csf3r*$^{-/-}$ uteri showed reduced nuclear accumulation of the G_1 cyclin-dependent kinase inhibitor p27^{kip1} within epithelial cells when compared to PL uteri. The panels show representative p27^{Kip1} immunostaining of uterine sections from 4-week-old mice (n ≥ 3 mice per group). Sections were co-stained for CK8 to visualize epithelial cells (top). In the PRPL section, note the loss of nuclear p27^{Kip1} in the epithelial compartment but not in the stroma. The bottom panels show p27^{Kip1} stain alone to accentuate the selective loss of p27^{Kip1} in the PRPL epithelium. (M) Gating strategy for tumor cell sorting prior to RNA-Seq analysis. Depicted cells were previously gated on total viable (7-AAD$^-$) cells. (N) Principle component analysis of RNA-Seq data. Note that PRPL and PRPL-*Csf3r*$^{-/-}$ groups cluster separately. (O) DAVID list of genes in GO Term 'Mitotic Cell Cycle' (see panel J) revealed in RNA-seq data to be up-regulated in PRPL versus PRPL-*Csf3r*$^{-/-}$ sorted tumor cells. (P) Identification of early apoptotic tumor cells using fluorescence inhibitor of caspases (FLICA) to detect cleaved caspase-3/7 in 4-week uteri. Contour plots (left) depict representative epithelial/tumor cells, gated as 7-AAD$^-$CD45$^-$Ly6G$^-$EpCAM$^+$ cells. Graph (right) shows mean ± SEM of one of two independent experiments with similar results (n ≥ 2 mice per group per experiment). *$p < 0.05$; ***$p < 0.005$. (Q, R) Representative cleaved caspase-3

(CC3)/CK8 and CC3/Ly6G immunostaining of serial uterine sections from 4-week-old mice (n ≥ 3 mice per group). The arrows and asterisk in the top right panel demarcate a large area of intraluminal debris. Note that $CC3^+$ cells are found in debris and intact epithelium alike, and that many $CK8^+$ tumor cells but few PMNs are $CC3^+$.

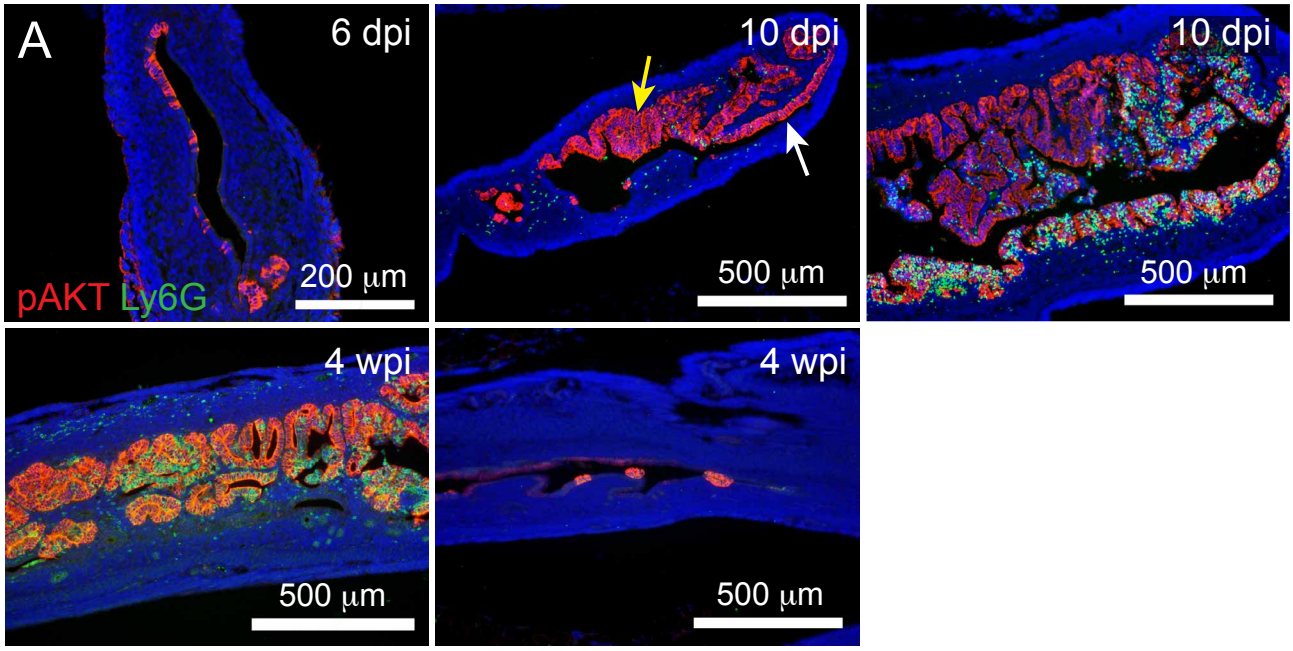
A
6 dpi
200 μm
pAKT Ly6G
10 dpi
500 μm
10 dpi
500 μm
4 wpi
500 μm
4 wpi
500 μm

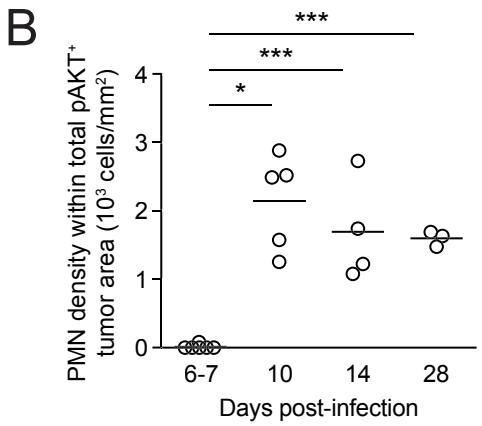
B
PMN density within total pAKT+ tumor area (10³ cells/mm²)
0
1
2
3
4
*
***
***
6-7
10
14
28
Days post-infection

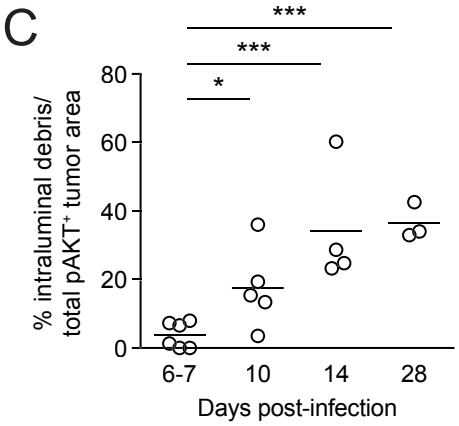
C
% intraluminal debris/ total pAKT+ tumor area
0
20
40
60
80
*
***
***
6-7
10
14
28
Days post-infection

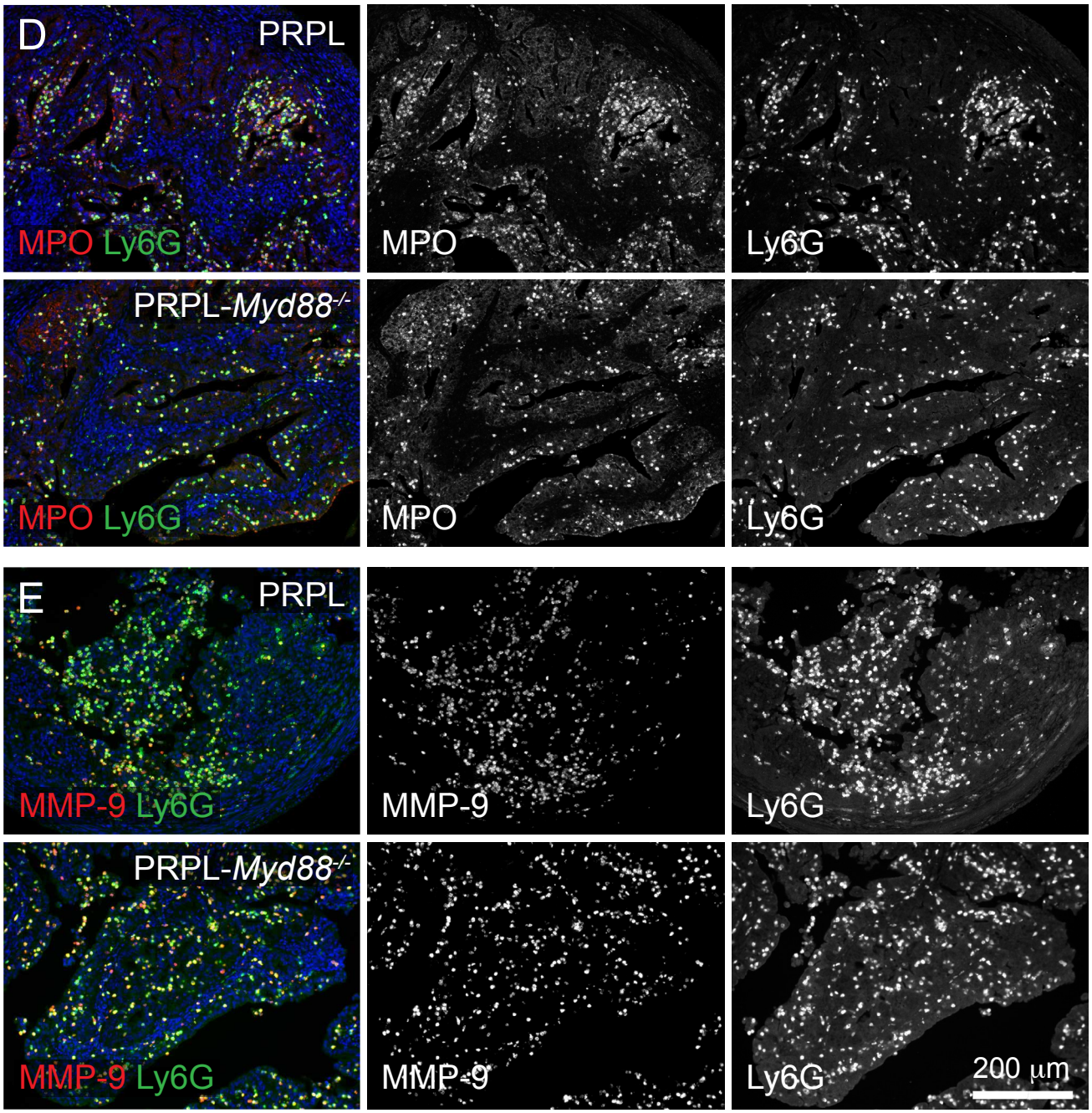
D
PRPL
MPO Ly6G
MPO
Ly6G
PRPL-Myd88-/-
MPO Ly6G
MPO
Ly6G
E
PRPL
MMP-9 Ly6G
MMP-9
Ly6G
PRPL-Myd88-/-
MMP-9 Ly6G
MMP-9
Ly6G
200 μm

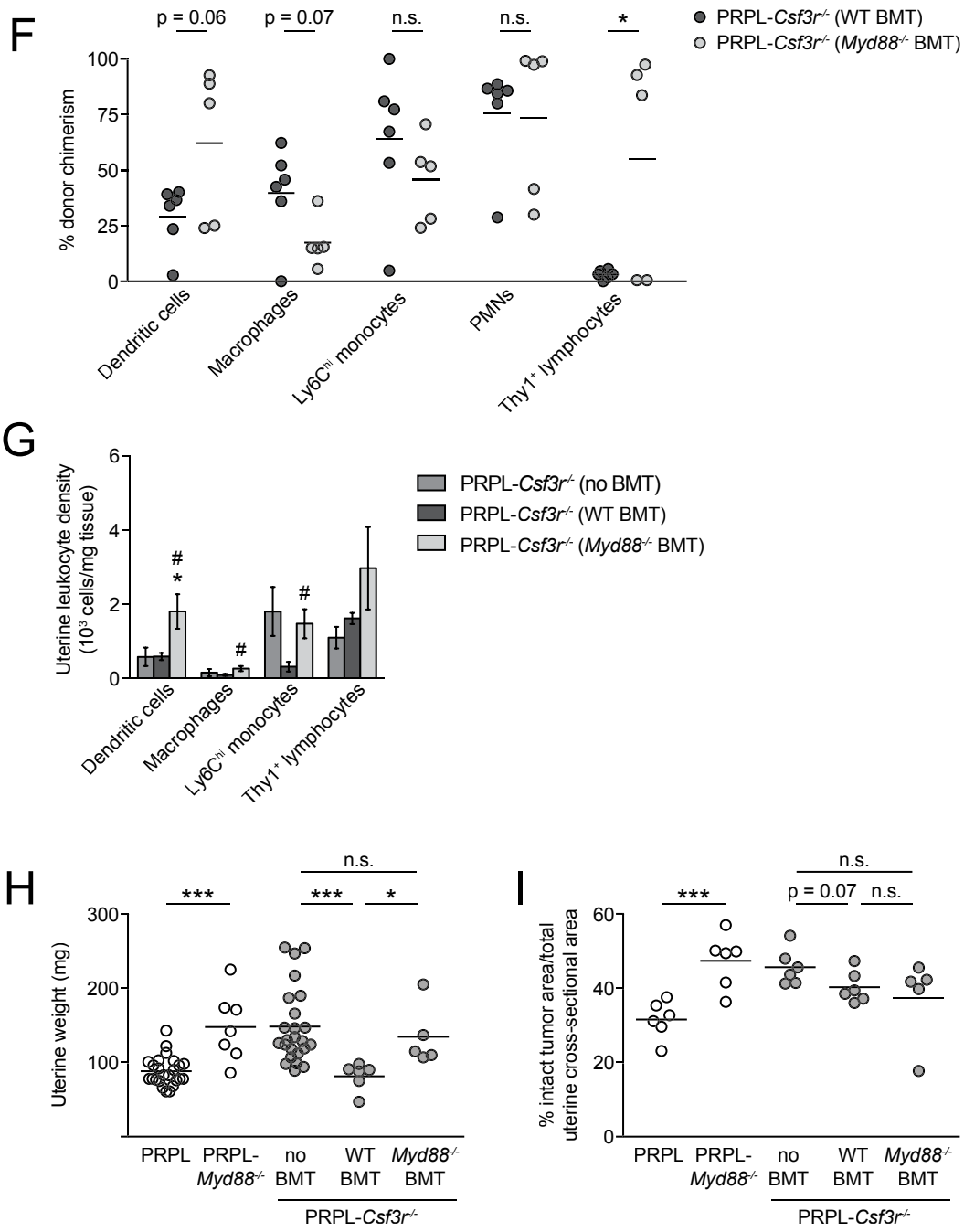
F
p = 0.06
p = 0.07
n.s.
n.s.
*
PRPL-Csf3r-/- (WT BMT)
PRPL-Csf3r-/- (Myd88-/- BMT)
% donor chimerism
100
75
50
25
0
Dendritic cells
Macrophages
Ly6Chi monocytes
PMNs
Thy1+ lymphocytes
G
Uterine leukocyte density (10³ cells/mg tissue)
6
4
2
0
PRPL-Csf3r-/- (no BMT)
PRPL-Csf3r-/- (WT BMT)
PRPL-Csf3r-/- (Myd88-/- BMT)
Dendritic cells
Macrophages
Ly6Chi monocytes
Thy1+ lymphocytes
H
Uterine weight (mg)
300
200
100
***
n.s.
***
*
PRPL
PRPL-Myd88-/-
no BMT
WT BMT
Myd88-/- BMT
PRPL-Csf3r-/-
I
% intact tumor area/total uterine cross-sectional area
60
40
20
0
***
n.s.
p = 0.07
n.s.
PRPL
PRPL-Myd88-/-
no BMT
WT BMT
Myd88-/- BMT
PRPL-Csf3r-/-

Figure S4, related to Figure 4. PMN activation and generation of PRPL-*Csf3r*$^{-/-}$ BMT mice. (A) Additional images of pAKT/Ly6G immunostaining of PL-AdCre uteri. At 6 days post-infection (dpi), pAKT^{+} lesions were nearly all PMN-free and formed largely flat, short segments interspersed within the otherwise normal uterine epithelium. At 10 dpi, some lesions remained flat (white arrow) and some had formed papillary structures (yellow arrow). The nascent tumor in the middle 10 dpi image has not yet been infiltrated with PMNs; the tumor in the right 10 dpi image shows partial PMN infiltration. At 4 weeks post-infection (wpi), most pAKT^{+} lesions were large, had invaginated into the endometrial stroma, and were infiltrated with PMNs (bottom left). However, 4 wpi uteri occasionally also contained small PMN-free pAKT^{+} lesions (bottom right). Representative images from n ≥ 3 mice per time point. (B) Time course of PMN density per total, pAKT^{+} tumor cross-sectional area, determined histologically in Ly6G/pAKT stained sections of PL-AdCre mice. (C) Time course of intraluminal debris generation in PL-AdCre mice. (D, E) MPO and MMP-9 immunostaining in 4-week PRPL and PRPL-*Myd88*$^{-/-}$ uteri. Note that both proteins co-localize with Ly6G^{+} PMNs and show similar staining intensities in PRPL versus PRPL-*Myd88*$^{-/-}$ uteri. Representative images from n ≥ 3 mice per group. (F) Chimerism of various leukocyte subsets in the uteri of 4-week-old PRPL-*Csf3r*$^{-/-}$ mice injected as neonates with bone marrow cells from the indicated sources. Chimerism was calculated by flow cytometry as the percentage of cells expressing the congenic mark (CD45.1 or CD45.2) that identified donor cells. (G) Uterine tissue densities of non-PMN leukocytes. *$p < 0.05$ versus PRPL-*Csf3r*$^{-/-}$ (no BMT); #$p < 0.05$ versus PRPL-*Csf3r*$^{-/-}$ (WT BMT). Data show mean ± SEM for n = 5-6 mice per group. (H, I) Uterine weight and percent uterine cross-sectional area comprised of intact tumor epithelium in the indicated 4-week-old mice. Tumor burden (Figure 4E) was calculated as the product of these two parameters since the latter represents the proportion of the entire uterus occupied by living tumor. PRPL and PRPL-*Csf3r*$^{-/-}$ (no BMT) data are the same as in Figure 2. *$p < 0.05$; ***$p < 0.005$.

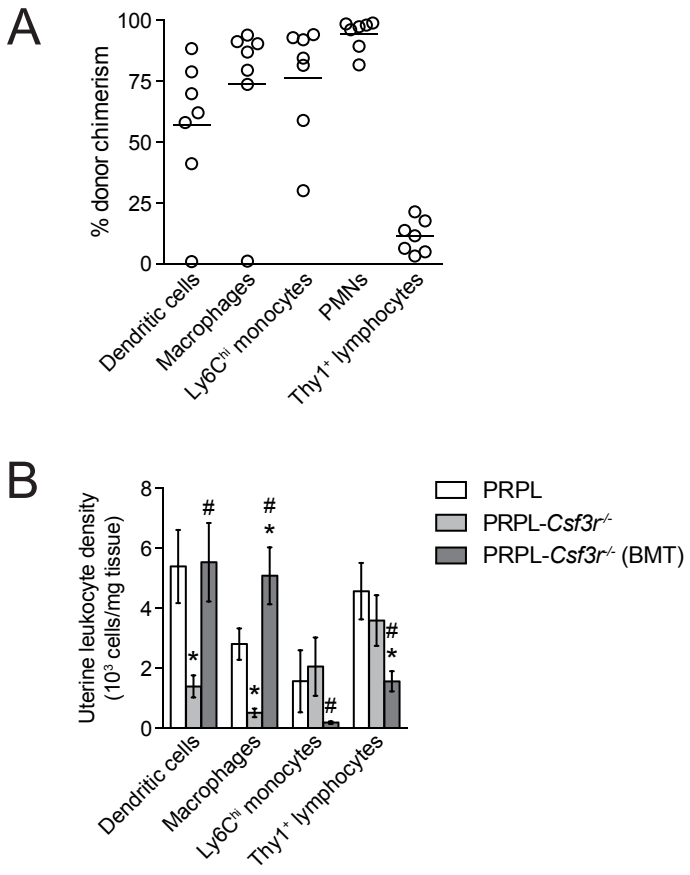

Figure S5, related to Figure 5. Chimerism and uterine leukocyte tissue densities in 12-week-old PRPL-*Csf3r*$^{-/-}$ (BMT) mice. (A) Chimerism of various uterine leukocyte subsets calculated by flow cytometry as the percentage of cells expressing the donor-derived CD45.1 congenic mark. (B) Uterine leukocyte densities, as determined by flow cytometry. *p < 0.05 versus PRPL; #p < 0.05 versus PRPL-*Csf3r*$^{-/-}$. Of note, the uterine densities of Ly6C^{hi} monocytes, the main other hematopoetic lineage known to express G-CSFR (Christopher et al., 2011), were modestly reduced in PRPL-*Csf3r*$^{-/-}$ (BMT) mice.

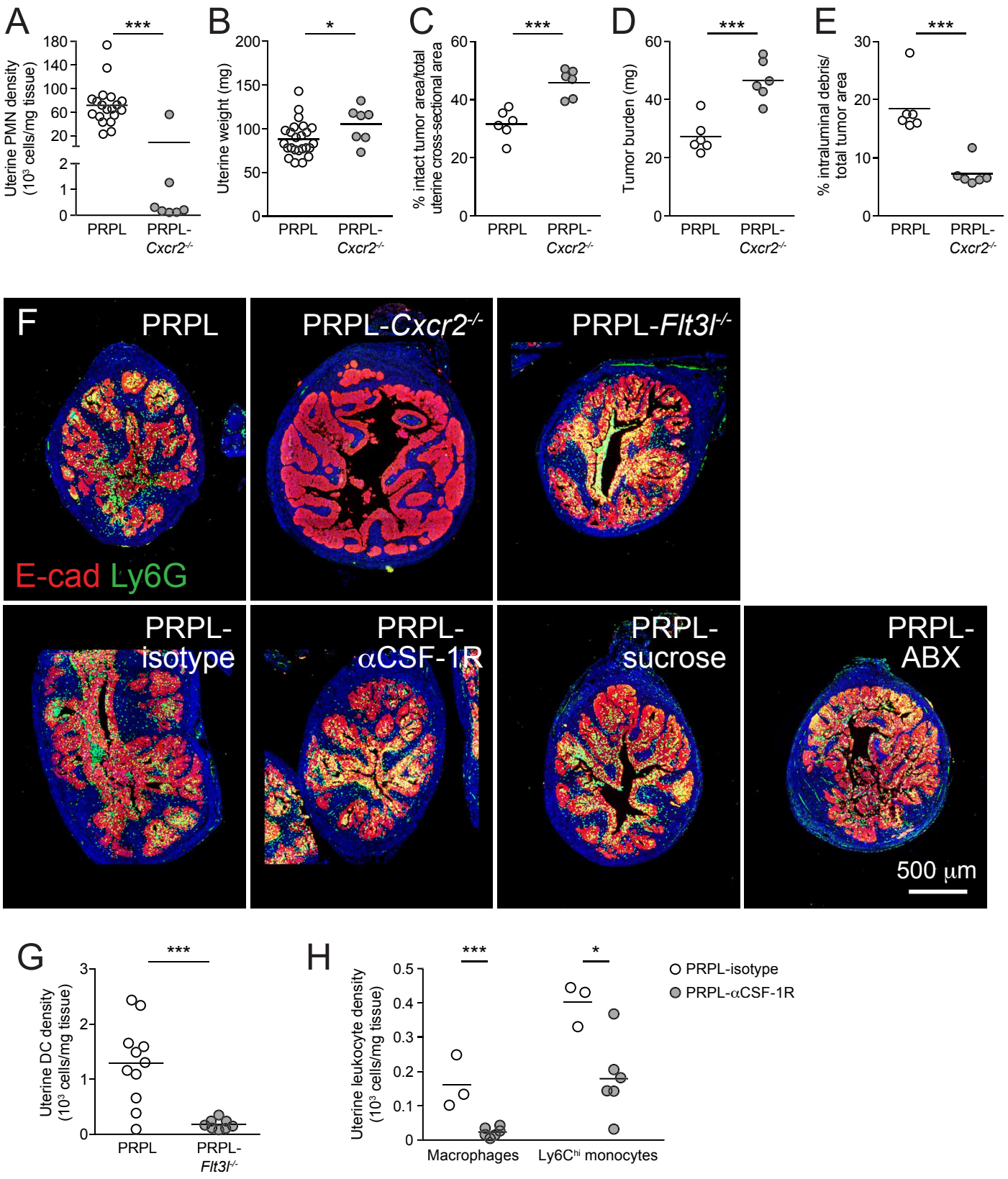
A
Uterine PMN density (10³ cells/mg tissue)
***
PRPL
PRPL-Cxcr2-/-
B
Uterine weight (mg)
*
C
% intact tumor area/total uterine cross-sectional area
***
D
Tumor burden (mg)
***
E
% intraluminal debris/ total tumor area
***
F
PRPL
PRPL-Cxcr2-/-
PRPL-Flt3l-/-
E-cad Ly6G
PRPL-isotype
PRPL-αCSF-1R
PRPL-sucrose
PRPL-ABX
500 μm
G
Uterine DC density (10³ cells/mg tissue)
***
PRPL
PRPL-Flt3l-/-
H
Uterine leukocyte density (10³ cells/mg tissue)
***
*
Macrophages
Ly6Chi monocytes
PRPL-isotype
PRPL-αCSF-1R

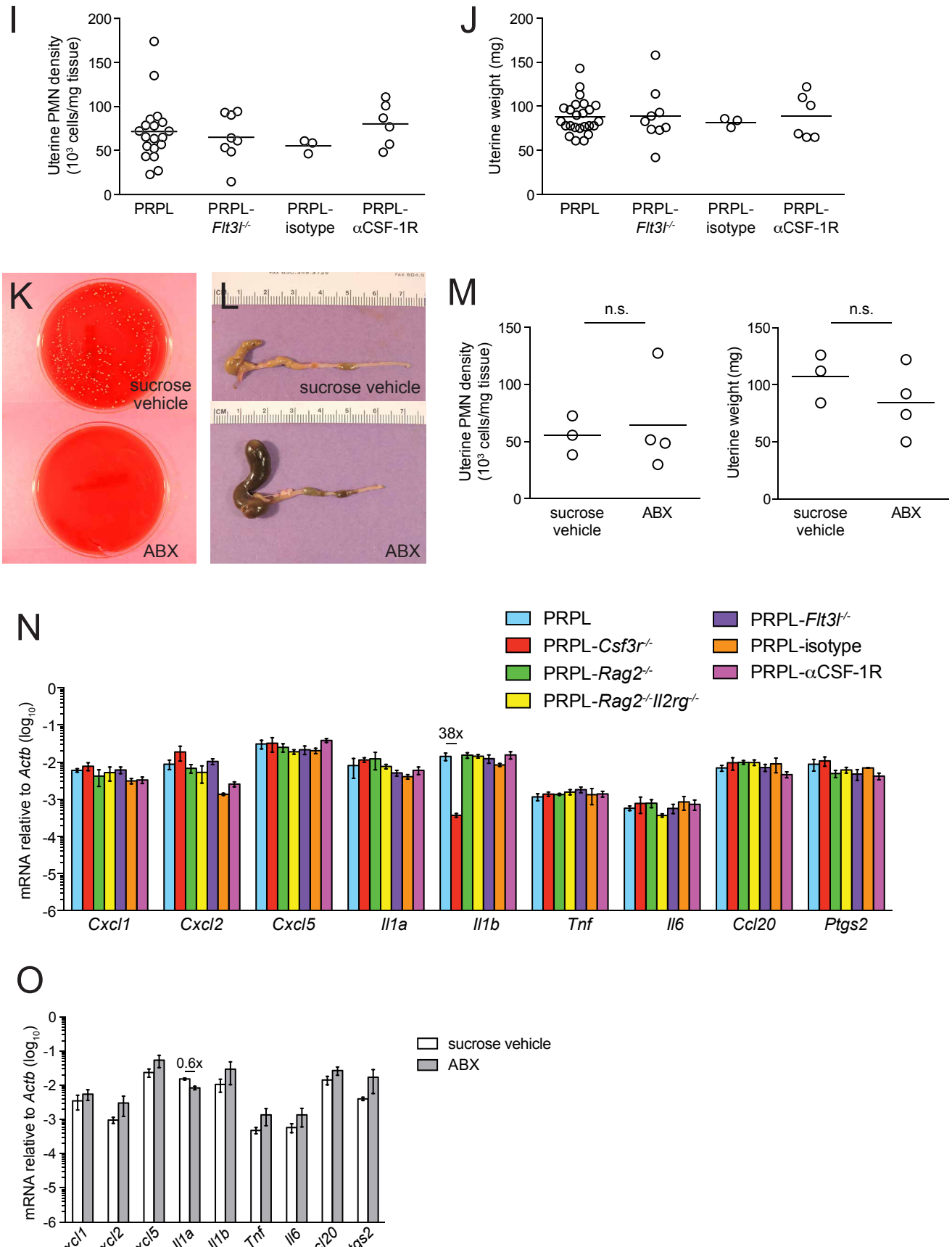
I
Uterine PMN density (10³ cells/mg tissue)
200
150
100
50
0
PRPL
PRPL-Flt3l-/-
PRPL-isotype
PRPL-αCSF-1R
J
Uterine weight (mg)
200
150
100
50
0
PRPL
PRPL-Flt3l-/-
PRPL-isotype
PRPL-αCSF-1R
K
sucrose vehicle
ABX
L
sucrose vehicle
ABX
M
n.s.
Uterine PMN density (10³ cells/mg tissue)
150
100
50
0
sucrose vehicle
ABX
n.s.
Uterine weight (mg)
150
100
50
0
sucrose vehicle
ABX
N
PRPL
PRPL-Csf3r-/-
PRPL-Rag2-/-
PRPL-Rag2-/-Il2rg-/-
PRPL-Flt3l-/-
PRPL-isotype
PRPL-αCSF-1R
mRNA relative to Actb (log10)
0
-1
-2
-3
-4
-5
-6
38x
Cxcl1
Cxcl2
Cxcl5
Il1a
Il1b
Tnf
Il6
Ccl20
Ptgs2
O
mRNA relative to Actb (log10)
0
-1
-2
-3
-4
-5
-6
0.6x
sucrose vehicle
ABX
Cxcl1
Cxcl2
Cxcl5
Il1a
Il1b
Tnf
Il6
Ccl20
Ptgs2

Figure S6, related to Figure 6. Further analysis of tumor cell-extrinsic stimuli on PMN recruitment and function. (A-E) Uterine PMN densities, weights, percent cross-sectional area comprised of intact tumor epithelium, tumor burden (uterine weight X % cross-sectional area comprised of intact tumor epithelium), and prevalence of intraluminal debris of total tumor area (intact epithelium plus debris) in 4-week-old PRPL and PRPL-*Cxcr2*$^{-/-}$ mice. The PRPL mice shown are the same ones analyzed in Figure 2. *$p < 0.05$; ***$p < 0.005$. (F) Representative E-cad/Ly6G immunostained uterine sections from 4-week-old mice depleted of various leukocyte subsets. Note the PRPL-*Cxcr2*$^{-/-}$ uterus lacks Ly6G^{+} PMNs but does not have as striking a papillary morphology as PRPL-*Csf3r*$^{-/-}$ uteri (see Figure 2E), suggesting a role for CXCR2 in PRPL tumorigenesis outside of PMN trafficking (e.g. Reutershan et al., 2006). Representative of $n \geq 3$ mice per group. (G) Demonstration of uterine DC deficiency in 4-week-old PRPL-*Flt3l*$^{-/-}$ mice. Values indicate the sum of CD11b^{lo} and CD11b^{hi} DC subsets, both of which were individually also significantly reduced in PRPL-*Flt3l*$^{-/-}$ uteri (not shown). PRPL data is the same as that used for Figure S2A. ***$p < 0.005$. (H) Demonstration of uterine macrophage and Ly6C^{hi} monocyte depletion in 4-week-old PRPL mice following treatment with antibodies to CSF-1R (PRPL-αCSF-1R) from postnatal day 14 versus PRPL mice treated with isotype control antibodies (PRPL-isotype). *$p < 0.05$; ***$p < 0.005$. (I, J) Uterine PMN densities and weights in 4-week-old mice. No differences are significant. (K) Demonstration of reduced gut flora in antibiotics-treated (ABX) 4-week-old PRPL mice when compared to sucrose vehicle-treated PRPL mice. 10 mg fecal pellet was homogenized in 1 ml PBS and 50 μl of a 10^6-fold dilution was plated on sheep's blood agar and incubated overnight at 37° C. (L) Representative gross images of cecum and colon from 4-week-old ABX- versus sucrose vehicle-treated PRPL mice. Note the substantially enlarged cecum in ABX-treated mice, indicative of commensal microbe depletion. (M) PMN density and weight of 4-week-old ABX- versus sucrose-treated uteri. (N, O) qRT-PCR analysis of ELR-CXC chemokine and other inflammatory gene expression in 4-week whole uteri. Data show mean ± SEM for $n \geq 3$ mice per group. Significant differences ($p < 0.05$) are indicated as fold change. PRPL data set in panel N is the same as in Figure 6A.

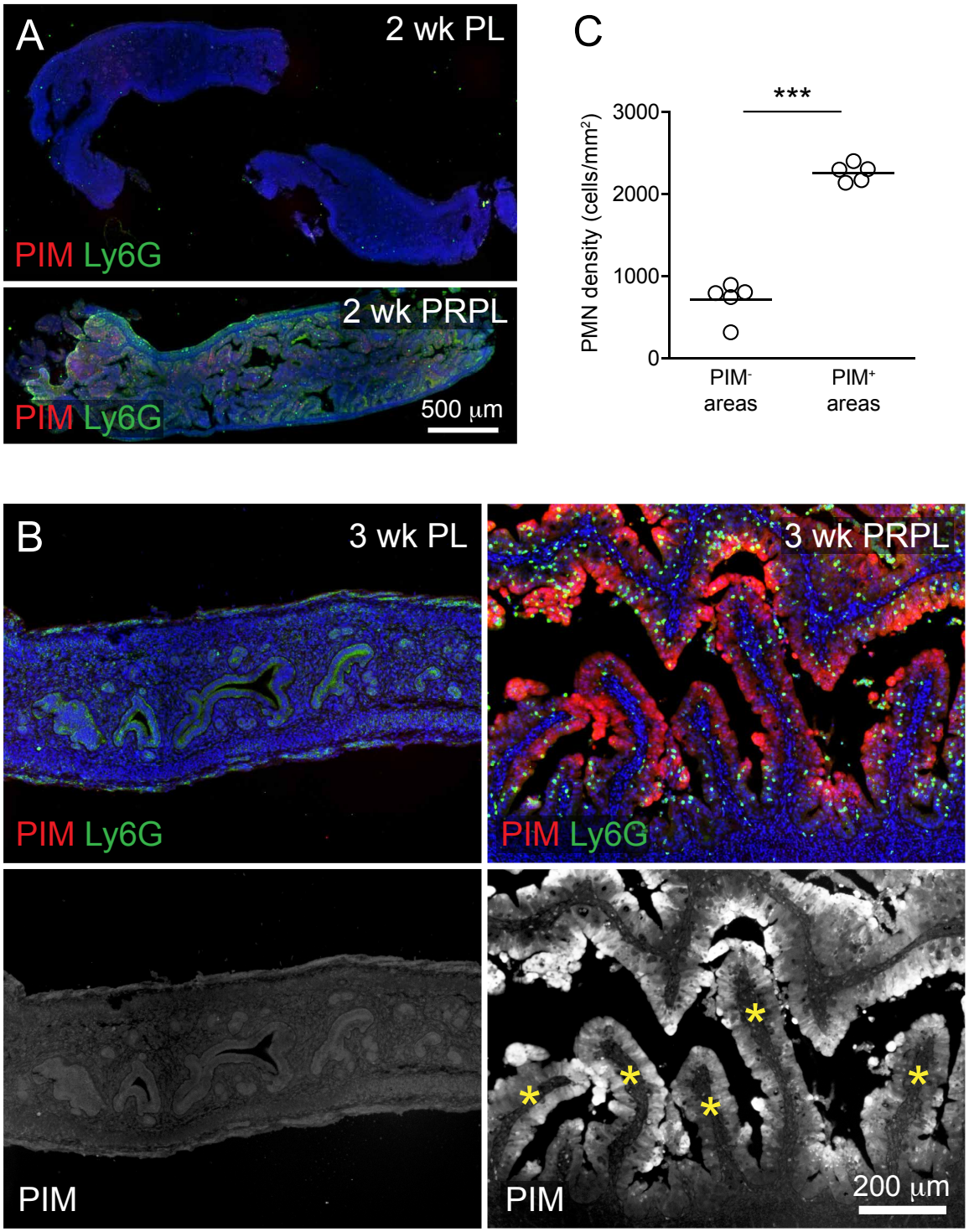
A
2 wk PL
PIM Ly6G
2 wk PRPL
PIM Ly6G
500 μm
C
***
PMN density (cells/mm²)
3000
2000
1000
0
PIM⁻ areas
PIM⁺ areas
B
3 wk PL
PIM Ly6G
3 wk PRPL
PIM Ly6G
PIM
PIM
200 μm

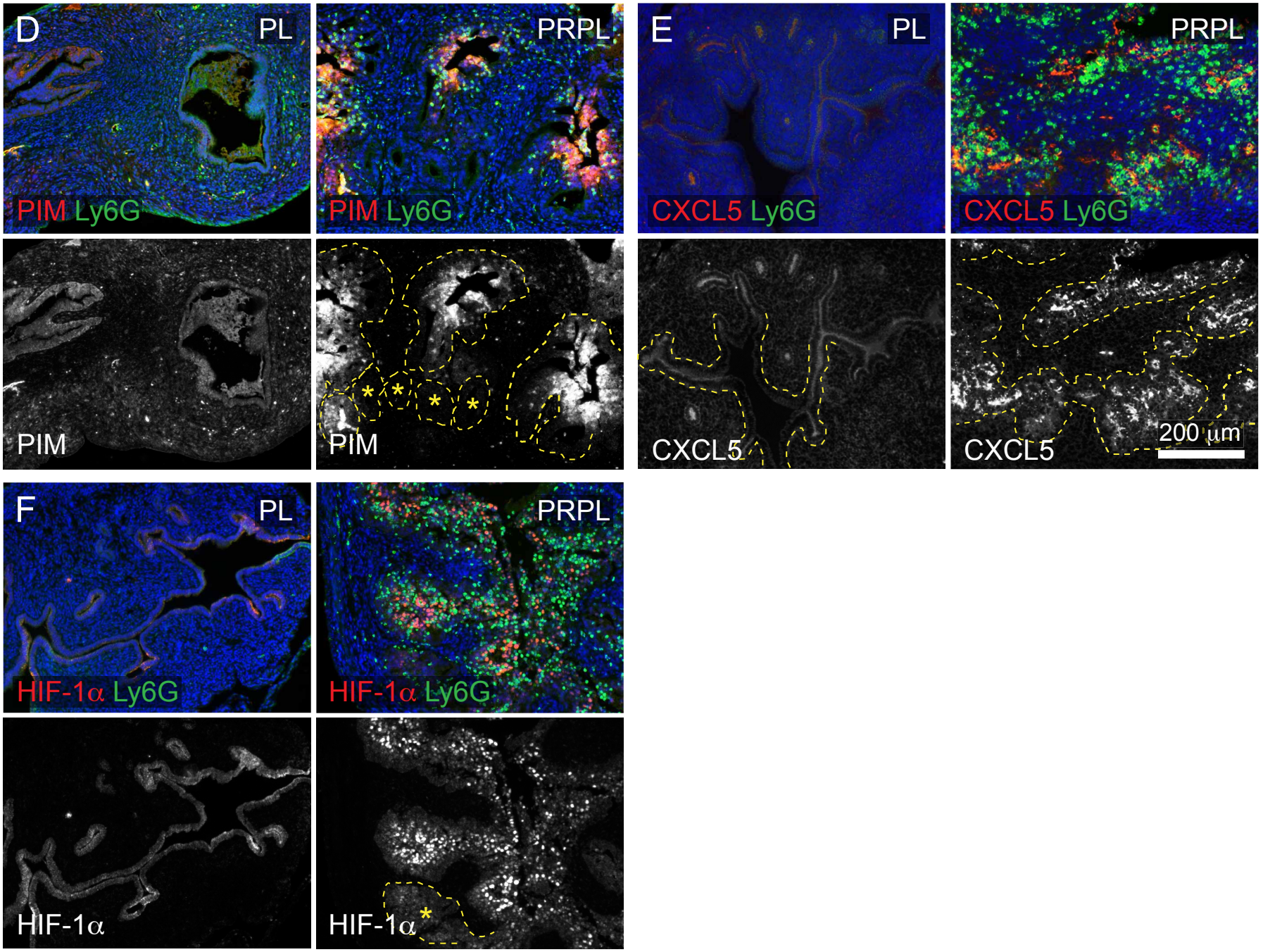
D
PL
PRPL
PIM Ly6G
PIM Ly6G
PIM
PIM
E
PL
PRPL
CXCL5 Ly6G
CXCL5 Ly6G
CXCL5
CXCL5
200 μm
F
PL
PRPL
HIF-1α Ly6G
HIF-1α Ly6G
HIF-1α
HIF-1α

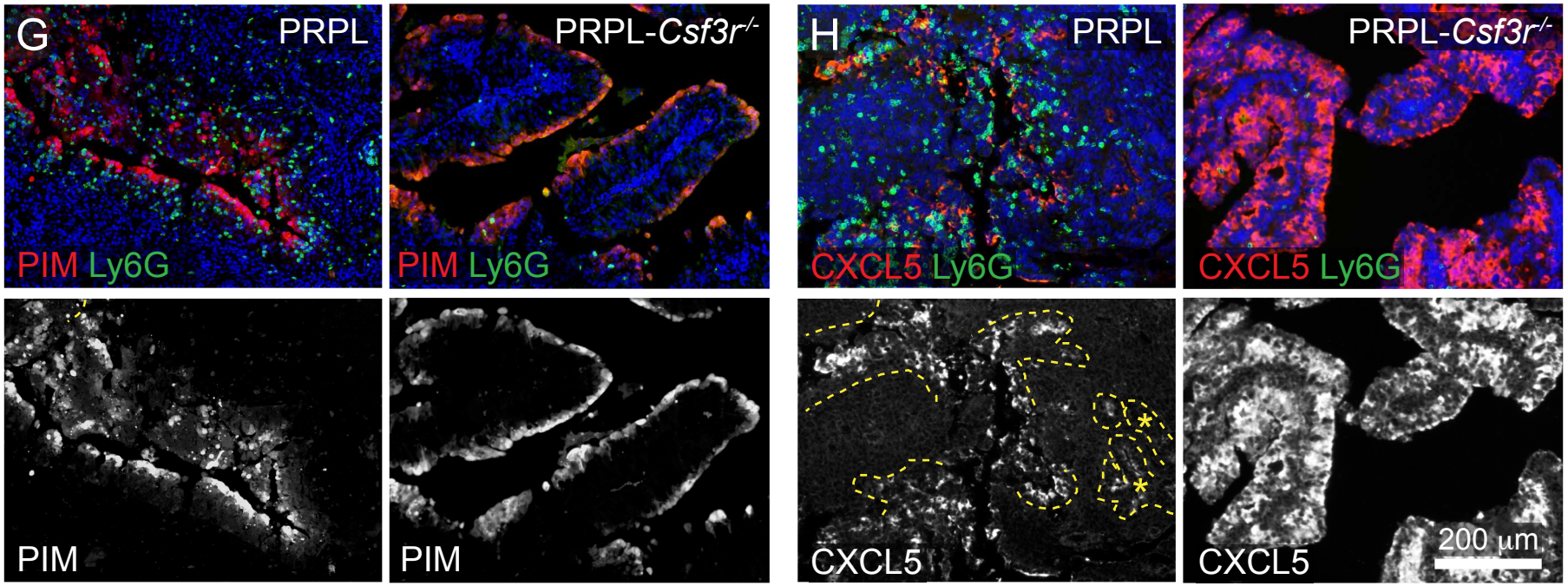
G
PRPL
PRPL-Csf3r-/-
PIM Ly6G
PIM Ly6G
PIM
PIM
H
PRPL
PRPL-Csf3r-/-
CXCL5 Ly6G
CXCL5 Ly6G
CXCL5
CXCL5
200 μm

I

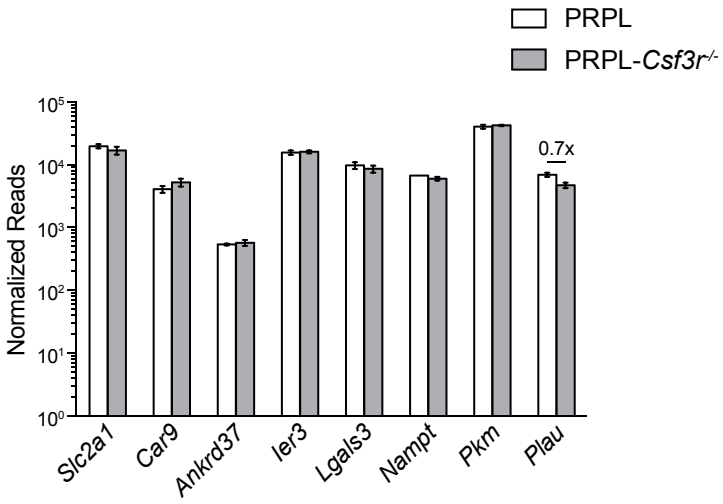
PRPL
PRPL-Csf3r-/-
Normalized Reads
0.7x
Slc2a1
Car9
Ankrd37
Ier3
Lgals3
Nampt
Pkm
Plau

Figure S7, related to Figure 7. Additional images and analysis documenting the spatial relationship between PMNs, uterine hypoxia and inflammation. In order to ensure controlled comparisons, the section of interest and its paired control for every panel set were from specimens that were fixed and processed at the same time and then embedded within the same paraffin block. Following immunostaining, the images were captured off of the same slide and at the same exposure. Brightness and contrast manipulations were then applied in the same way to paired images. When not obvious, the border between the epithelium and stroma is demarcated with dashed yellow lines. All images are representative of n ≥ 3 mice per group. (A) PIM/Ly6G immunostained uterine sections from paired 2-week-old mice. The diffuse green staining in the PRPL image is non-specific background. (B) Close-up of the PIM/Ly6G immunostained uterine sections from the paired 3-week-old mice shown in Figures 7A and 7B. Note the PIM^+ staining throughout the epithelium of the PRPL uterus, even in areas organized into papillary structures (asterisks). These latter areas are relatively PMN-free. (C) PMN densities in hypoxic (PIM^+) versus non-hypoxic (PIM^-) tumor foci in 4-week PRPL uteri. ***$p < 0.005$. (D-F) PIM/Ly6G, CXCL5/Ly6G, and HIF-1α/Ly6G immunostaining of paired 4-week PL and PRPL sections. Some tumor foci lacking PMNs are indicated with asterisks. (G-H) PIM/Ly6G and CXCL5/Ly6G immunostaining of paired 4-week PRPL and PRPL-*Csf3r*$^{-/-}$ sections. (I) RNA-seq data of hypoxia-induced genes in 4-week PRPL versus PRPL-*Csf3r*$^{-/-}$ sorted tumor cells (n = 3-4 samples per group). Significant difference ($p < 0.05$) is indicated as fold change.

A

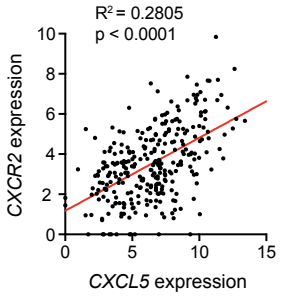

B

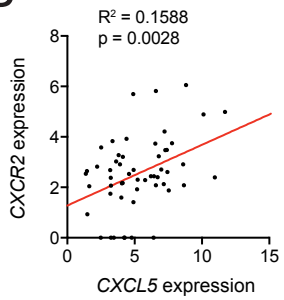

C

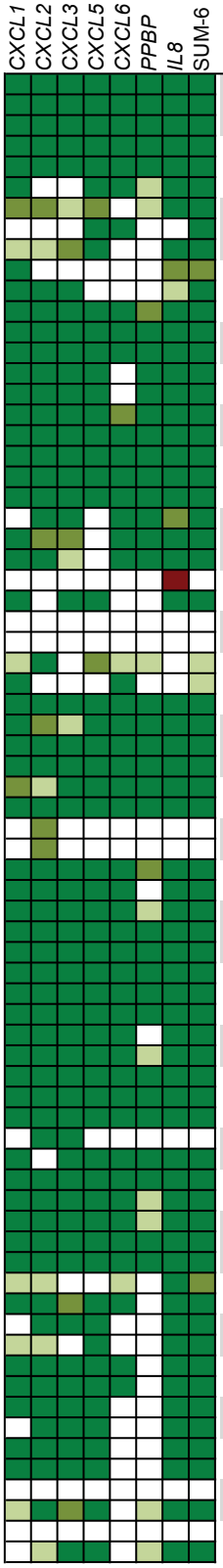

PMN Marker	TISSUE	HISTOLOGICAL TYPE
CSF3R CXCR2 FCGR3B	PAN-CANCER	All primary solid tumors (n=6044)
CSF3R CXCR2 FCGR3B	UTERUS	Endometrioid adenocarcinoma (n=295)
CSF3R CXCR2 FCGR3B	UTERUS	Serous adenocarcinoma (n=54)
CSF3R CXCR2 FCGR3B	UTERUS	Carcinosarcoma, all Subtypes (n=57)
CSF3R FCGR3B	ADRENAL	Adrenocortical carcinoma (n=69)
CSF3R FCGR3B	ADRENAL	Pheochromocytoma (n=91)
CSF3R FCGR3B	BLADDER	Urothelial carcinoma (n=222)
CSF3R CXCR2 FCGR3B	BRAIN	Glioblastoma multiforme (n=152)
CSF3R CXCR2 FCGR3B	BRAIN	Lower grade glioma (n=397)
CSF3R FCGR3B	BREAST	Ductal carcinoma (n=699)
CSF3R FCGR3B	BREAST	Lobular carcinoma (n=157)
CSF3R CXCR2 FCGR3B	CERVIX	Squamous cell carcinoma (n=168)
CSF3R CXCR2 FCGR3B	COLON/RECTUM	Adenocarcinoma (n=295)
CSF3R FCGR3B	ESOPHAGUS	Adenocarcinoma (n=43)
CSF3R FCGR3B	ESOPHAGUS	Squamous cell Carcinoma (n=48)
CSF3R FCGR3B	HEAD/NECK	Squamous Cell Carcinoma (n=407)
CSF3R CXCR2 FCGR3B	KIDNEY	Clear cell carcinoma (n=499)
CSF3R CXCR2 FCGR3B	KIDNEY	Papillary cell carcinoma (n=203)
CSF3R FCGR3B	KIDNEY	Chromophobe renal cell carcinoma (n=57)
CSF3R CXCR2 FCGR3B	LIVER	Hepatocellular carcinoma (n=155)
CSF3R FCGR3B	LUNG	Adenocarcinoma NOS (n=264)
CSF3R FCGR3B	LUNG	Squamous cell carcinoma (n=362)
CSF3R CXCR2 FCGR3B	MESENCHYME	Sarcoma, all subtypes (n=118)
CSF3R FCGR3B	OVARY	Serous cystadenocarcinoma (n=254)
CSF3R FCGR3B	PANCREAS	Ductal adenocarcinoma (n=77)
CSF3R FCGR3B	PROSTATE	Acinar adenocarcinoma (n=232)
CSF3R FCGR3B	SKIN	Melanoma** (n=269)
CSF3R FCGR3B	STOMACH	Adenocarcinoma NOS (n=127)
CSF3R FCGR3B	THYROID	Classical/usual papillary carcinoma (n=323)
CSF3R FCGR3B	THYROID	Follicular papillary carcinoma (n=96)

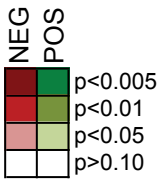

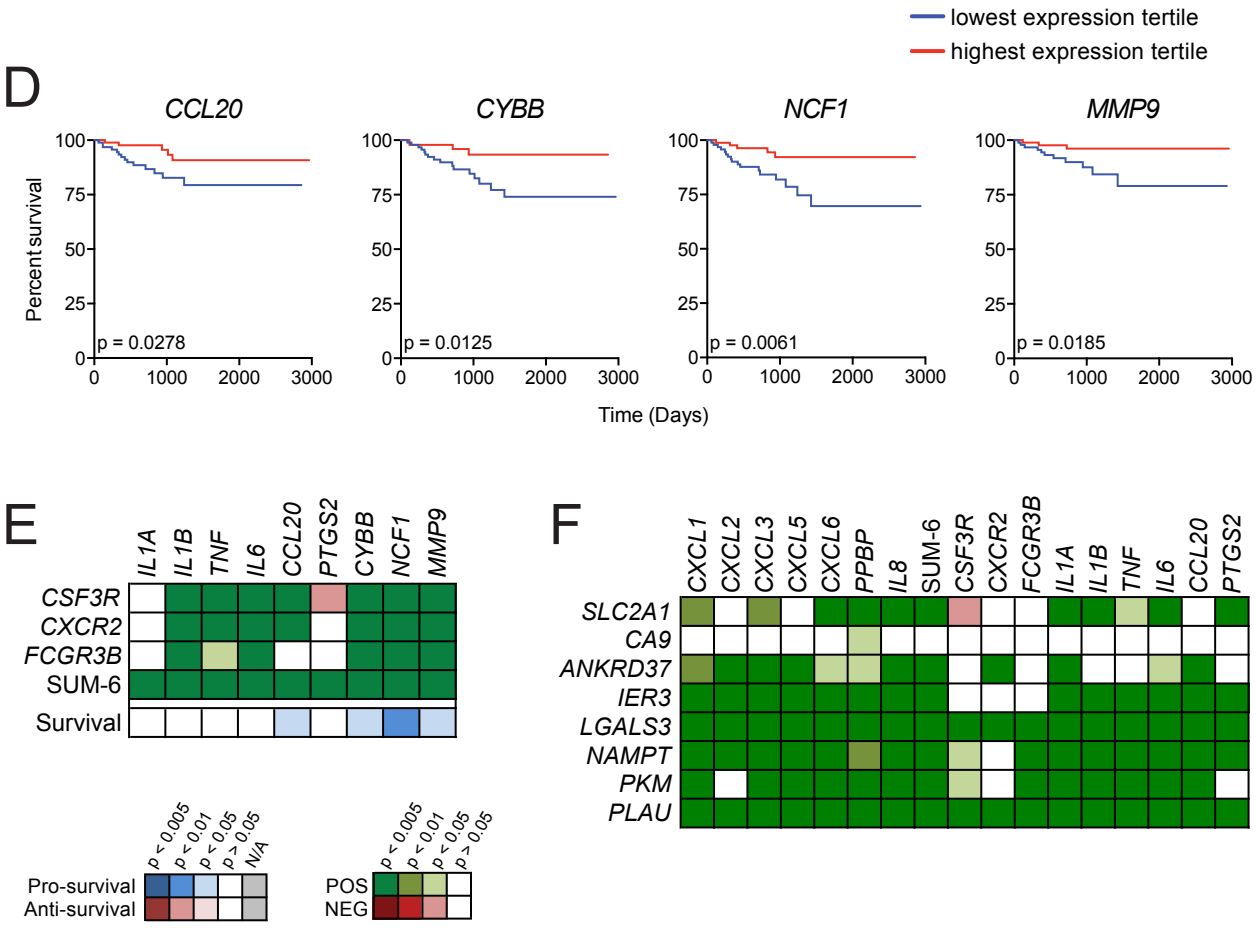
D
lowest expression tertile
highest expression tertile
CCL20
CYBB
NCF1
MMP9
Percent survival
p = 0.0278
p = 0.0125
p = 0.0061
p = 0.0185
Time (Days)
E
IL1A
IL1B
TNF
IL6
CCL20
PTGS2
CYBB
NCF1
MMP9
CSF3R
CXCR2
FCGR3B
SUM-6
Survival
p < 0.005
p < 0.01
p < 0.05
p > 0.05
N/A
Pro-survival
Anti-survival
POS
NEG
F
CXCL1
CXCL2
CXCL3
CXCL5
CXCL6
PPBP
IL8
SUM-6
CSF3R
CXCR2
FCGR3B
IL1A
IL1B
TNF
IL6
CCL20
PTGS2
SLC2A1
CA9
ANKRD37
IER3
LGALS3
NAMPT
PKM
PLAU

Figure S8, related to Figure 8. Correlation of hypoxia, inflammation, PMN infiltration and survival outcome in human cancers. (A, B) Representative linear regression analyses from TCGA RNA-seq data comparing tumor expression of an ELR-CXC chemokine gene (*CXCL5*) with a PMN-specific gene (*CXCR2*) in endometrioid EC (A) and serous EC (B). (C) Correlation of ELR-CXC chemokine and PMN-specific gene expression across many human cancers. Heat map represents p values from linear regression analyses, like those in panels A and B, across the indicated cancer subtypes. ELR-CXC chemokine genes and SUM-6 are listed along the top, while PMN-specific genes are indicated on the right. Green shaded boxes denote a significant ($p < 0.05$) positive (POS) correlation in expression for a given pair of genes; red shaded boxes denote a significant negative (NEG) correlation in expression; white boxes denote no significant correlation in either direction ($p > 0.05$). Analyses using *CXCR2* were not possible for certain cancer subtypes because their datasets contained many samples with negligible *CXCR2* expression. Cancer tissue of origin, histological type and sample size are indicated on the right. (D) Survival analysis of PMN effector genes (*CYBB*, *NCF1*, *MMP9*) and the pro-inflammatory gene *CCL20* in human endometrioid EC, performed as in Figure 8A. (E) Correlation of the PMN signature (left) with the expression of other inflammatory and PMN effector genes (top) in human endometrioid EC. Heat map generated as in panel C. Bottom row indicates impact of each inflammatory and PMN effector gene (top) on survival outcome, as in Figure 8B. (F) Expressional correlation of hypoxia-induced genes (left) with PMN signature and other inflammatory genes (top) in human endometrioid EC. Heat map generated as in panel C.

SUPPLEMENTAL EXPERIMENTAL PROCEDURES

Bone marrow transfer (BMT). Bone marrow harvested from femurs and tibias of 8-12-week-old mice was re-suspended in PBS to a concentration of 1.5-4 x 10^8 cells/ml and injected (1.5-4 x 10^7 total) i.p. into neonatal (postnatal days 4-10) recipients. These recipients did not receive myeloablative irradiation or chemotherapy. For WT BMT, donor cells were taken from C57BL/6 CD45.1 mice (B6.SJL-*Ptprc*^{a}/BoyAiTac; Taconic, model 4007) and injected into PRPL-*Csf3r*$^{-/-}$ (CD45.2) recipients. For *Myd88*$^{-/-}$ BMT, donor cells were taken from *Myd88*$^{-/-}$ mice (CD45.2) and injected into PRPL-*Csf3r*$^{-/-}$ recipients that had been crossed onto a CD45.1 background.

Treatments. For G-CSF neutralization, PRPL female mice were given daily intraperitoneal (i.p.) injections of 8 μg monoclonal rat anti-mouse G-CSF (R&D Systems; clone 67604) or rat IgG_1 isotype control (BioXCell; HPRN) from postnatal day 19 (P19) until sacrifice on P28. For macrophage and monocyte depletion, PRPL females were given i.p. injections of 100 μg monoclonal rat anti-mouse CSF-1R (BioXCell; AFS98) or rat IgG2a isotype control (BioXCell; 2A3) every other day from P14 until sacrifice on P28. For *in situ* proliferation studies, females were injected i.p. with 2 mg 5-bromo-2'-deoxyuridine (BrdU; Fisher Scientific) 2 hr prior to sacrifice. For *in situ* detection of hypoxia, mice were injected i.p. with 0.75 mg pimonidazole hydrochloride (Hypoxyprobe) 1.5 hr prior to sacrifice. Antibiotics treatment (1 mg/ml ampicillin; 1 mg/ml metronidazole; 1 mg/ml neomycin; 0.5 mg/ml vancomycin) was administered along with 1% sucrose in the drinking water of pregnant mice bearing PRPL pups beginning approximately 1 week prior to birth until sacrifice at 4 weeks of age. Control mice received drinking water with 1% sucrose only. Mice sacrificed at 8 or 12 weeks of age were injected subcutaneously with 2 mg progesterone (Sigma-Aldrich) diluted in sesame oil once daily for 3 days prior to sacrifice in order to normalize the effects of the estrus cycle on uterine morphology and leukocyte composition.

Adenoviral infection. Bilateral ovariectomy was performed on 4-week-old PL female mice. Two weeks post-surgery, mice were injected transcervically with 1.0 x 10^9 pfu Adeno-Cre/GFP (University of Iowa Viral Vector Core) diluted in 10 μl MEM. Injection was performed using a 10 ml Hamilton syringe with attached PE-10 polyethylene tubing (BD Biosciences) to blunt the needle as previously described (Collins et al., 2009).

Cell culture. ECC-1, Ishikawa, RL95-2, HEC-1A, HEC-1B and KLE human endometrial carcinoma cell lines were the gifts of Dr. Gottfried Konecny (UCLA Medical Center, Santa Monica, CA). Cells were cultured in DMEM (Corning) supplemented with 10% FBS (Atlanta Biologicals), 10 mM HEPES buffer, 2 mM L-glutamine, 100 IU/ml penicillin, 100 μg/ml streptomycin, 1 mM sodium pyruvate and MEM non-essential amino acids (Corning). Cells were maintained at 37°C, 5% CO_2 and ambient oxygen (~21% O_2). For hypoxia studies, cells were plated in triplicate within two separate 24-well plates at ~5.0 x 10^5 cells/well. After 24 h, one plate of cells was transferred to a Heracell 150i incubator (Thermo Scientific) adjusted to 1% O_2 while the other plate was maintained in ambient oxygen. Cells were cultured for an additional 48 hr prior to RNA isolation.

Preparation and analysis of mouse tissue. For flow cytometric analysis, dissected whole uterine tissue was digested as previously described (Collins et al., 2009). Briefly, uteri were minced and re-suspended in Hank's Balanced Salt Solution (HBSS) containing 0.28 Wünsch units/ml Liberase TM Research Grade (Roche Life Science) and 30 μg/ml DNAase I (Roche), then incubated for 30 min at 37°C with intermittent trituration. Tissues were washed and then re-suspended in FACS buffer (PBS, 1% FBS, 5 mM EDTA) and incubated at 37°C for an additional 15 min, after which they were filtered through 70 μm nylon mesh. For analyses of blood and bone marrow, cells were harvested and processed exactly as uterine tissue without prior erythrocyte lysis to avoid potential activating effect on PMNs.

For basic cell surface staining, ~2.0 x 10^6 cells were exposed to 10 μg/ml rat anti-mouse CD16/CD32 (BioXCell; 2.4G2) to block non-specific binding. Cells were then stained with the appropriate cocktail of fluorochrome-conjugated primary antibodies (see Supplemental Experimental Tables), and lastly were treated with 5 μg/ml 7-aminoactinomycin D (7-AAD; BD Pharmingen) for live/dead discrimination. Samples were analyzed using a 10-color 3-laser BD LSR II flow cytometer. Viable leukocyte ($CD45^+7\text{-}AAD^-$) numbers were determined following doublet discrimination using FCS Express (De Novo Software), and were further divided into subsets using the gating strategies in Figure S1B. To calculate leukocyte subset densities, the percentage of a given leukocyte subset among total viable ($7\text{-}AAD^-$) singlet cells was multiplied by the total number of cells counted in the sample (Trypan Blue exclusion), then divided by the weight of the digested tissue. Dot plots and histograms for figures were generated using FlowJo (Tree Star, Inc.). Blood samples were additionally lysed using ACK Lysing Buffer (Lonza) and re-filtered immediately prior to acquisition.

Flow cytometry antibodies.

Antigen	Company	Clone	Catalog No.	Fluorochrome
α6	Biolegend	GoH3	313615	APC
β1	Biolegend	HMβ1-1	102215	APC
β4	Biolegend	346-11A	123605	FITC
CD4	Biolegend	GK1.5	100414	APC/Cy7
CD8α	Biolegend	53-6.7	100708	PE
CD11b	BD Pharmingen	M1/70	557657	APC/Cy7
CD11c	Biolegend	N418	117318	PE/Cy7
CD45	Biolegend	30-F11	103138	Brilliant Violet 510
CD45.1	BD Pharmingen	A20	553775	FITC
CD45.2	Biolegend	104	109830	PE/Cy7
F4/80	Biolegend	BM8	123116	APC
IL-1β	eBioscience	NJTEN3	17-7114-80	APC
Ly6C	BD Pharmingen	AL-21	553104	FITC
Ly6G	Biolegend	1A8	127622	Alexa Fluor 700
MHCII (I-A/I-E)	Biolegend	M5/114.15.2	107620	Pacific Blue
NK1.1	BD Pharmingen	PK136	552878	PE/Cy7
TCRβ	Biolegend	H57-597	109212	APC
TCRγδ	BD Pharmingen	GL3	553177	FITC
Thy1.2	Biolegend	53-2.1	140306	Pacific Blue

For IL-1β intracellular cytokine staining, ~2.0 x 10^6 digested uterine, blood or bone marrow cells were immediately fixed and permeabilized using the BD Cytofix/Cytoperm Kit (BD Biosciences) and subjected to cytokine staining according to the manufacturer's protocol. Fixed samples subsequently underwent cell surface staining with fluorochrome-conjugated antibodies as above, minus the 7-AAD staining step. For ROS studies, digested uterine, blood or bone marrow cells were re-suspended in RPMI containing 10% FBS and plated at 1.0 x 10^5 cells/well in a 96-well U-bottom plate either in the presence of 12.5 ng/ml dihydrorhodamine 123 (DHR; Life Technologies), DHR plus 20 ng/ml phorbol 12-myristate 13-acetate (PMA; Sigma-Aldrich), or vehicle control (DMSO). Cells were incubated for 30 min in a 37°C, 5% CO_2 incubator at ambient oxygen. Cells were then washed in FACS buffer, subjected to cell surface staining, and analyzed by flow cytometry as described above.

For fluorescent inhibitor of caspases (FLICA) studies, whole uteri were harvested, fileted open longitudinally, and cut crosswise into 0.5 cm strips. Tissue was then incubated in HBSS containing 0.5% trypsin (Corning) and the caspase 3/7 FLICA substrate (ImmunoChemistry Technologies) for 30 min at 37°C. Tissues were vortexed for 30 s to separate epithelial sheets, and the remaining uterine tissue was discarded. Epithelial cells were further disaggregated by trituration and incubation for 15 min in FACS buffer at 37°C, and analyzed by flow cytometry as above.

For *ex vivo* trypan blue vital staining, whole uteri were dissected and a 1.5 cm long segment from each horn was cut to expose the uterine lumen on both sides. A pipet tip containing 200 μl HBSS was inserted into the lumen at one end of the uterine segment and the luminal contents were gently flushed into a 1.7 ml centrifuge tube. The contents were centrifuged and the pellet was then re-suspended in a 100 μl solution of 1:1 PBS:0.4% Trypan Blue (Corning cellgro) and incubated at room temperature for 5 min. After washing in PBS, the pellet was then re-suspended in 100 μl PBS. Thin layer preparations were made using a Shandon Cytospin 3, and images were taken on a Nikon Eclipse 80i. The cells visualized in this fashion were either single cells or small cell clumps clearly distinct from the contiguous epithelial sheets that could be isolated via the trypsinization protocol described for FLICA staining in the above paragraph.

Immunofluorescence staining of uterine tissue sections. Freshly isolated uteri were fixed in 4% paraformaldehyde/PBS overnight (ON) at 4°C. Tissues were then embedded in paraffin and sectioned at 5 μm by the NYU School of Medicine Histopathology Core. Some slides were subjected to routine H&E staining. Immunofluorescence staining was performed as previously described (Blaisdell and Erlebacher, 2014). Briefly, deparaffinized slides were placed in methanol containing 3% H_2O_2 for 20 min. Depending upon the primary antibody (see Supplemental Experimental Tables), the tissues were then subjected to antigen retrieval either by incubation in 1 mg/ml trypsin in H_2O for 10 min at 37°C or by boiling in 0.01 M citric acid (pH 6.0) for 10-20 min in a pressure cooker. The slides were then blocked in 3% bovine serum albumin (BSA; Sigma-Aldrich) containing 3% donkey serum and 0.4% Triton X-100 (Sigma-Aldrich) for 1 hr at RT, and then incubated overnight at 4°C with primary antibodies diluted in PBS containing 1% BSA and 0.4% Triton X-100. The slides were washed in PBS and the sections were then labeled for 30 min at RT with secondary antibodies (Jackson ImmunoResearch) conjugated either to anti-rat Alexa Fluor 488 (for anti-CK8, anti-CK8 and anti-laminin γ1 staining) or horseradish peroxidase (HRP; all other primary antibodies aside from Pimonidazole staining) diluted to 5 mg/ml in TNB blocking buffer (PerkinElmer). Specimens labeled with HRP-conjugated secondary antibodies were subjected to tyramide signal amplification (TSA) in PBS containing 1.8 μg/ml biotin-tyramide (PerkinElmer) and 0.0015% H_2O_2 for 5 min at RT. The slides were finally labeled for 30 min at RT with a streptavidin-Alexa Fluor 594 conjugate (Jackson ImmunoResearch) diluted to 5 mg/ml in 1% BSA and counterstained with 4',6-diamidino-2-phenylindole (DAPI) diluted in H_2O. Pimonidazole staining was performed using a FITC-conjugated primary antibody (Hypoxyprobe) without amplification

and an anti-rat Alexa Fluor 594 secondary to visualize anti-Ly6G-stained cells. All immunofluorescent images were captured using an AxioImager M1 and AxioVision Rel. 4.8 software (Zeiss). Panoramic views were generated by tiling images taken at 100X magnification.

Tissue immunostaining antibodies/conditions

Antigen	Abbrev	Company	Catalog No.	Retrieval	Dilution	TSA*
α6	α6	Abcam	ab181551	Citrate	1:1000	Yes
β4	β4	Acris	217381-AP	Citrate	1:100	Yes
Bromodeoxyuridine	BrdU	BD Biosciences	550803e	Citrate	1:30	Yes
Cleaved caspase-3	CC3	Cell Signaling Technology	9661	Trypsin	1:1000	Yes
CXCL5	CXCL5	LifeSpan Biosciences	LS-C212192	Trypsin	1:1000	Yes
Cytokeratin-8	CK8	Univ of Iowa Developmental Studies Hybridoma Bank	Troma-1	Tryp/Cit	1:250	No
E-cadherin	E-cad	Cell Signaling Technology	3195	Citrate	1:1000	Yes
HIF-1α	HIF-1α	Novus Biologicals	NB100-479B	Citrate	1:1000	Yes
IL-1β	IL-1β	R&D Systems	AF-401-NA	Citrate	1:100	Yes
Laminin γ1	Laminin γ1	Abcam	Ab177792	Trypsin	1:100	No
Ly6G	Ly6G	BD Biosciences	551459	Tryp/Cit	1:250	No
$p27^{Kip1}$	$p27^{Kip1}$	Santa Cruz Biotechnology	sc-528	Citrate	1:3000	Yes
phospho-AKT (ser473)	pAKT	Cell Signaling Technology	4060	Trypsin	1:1000	Yes
phospho-histone H3	pH3	Cell Signaling Technology	9701	Citrate	1:1000	Yes
phospho-HP1γ (ser83)	pHP1γ	Abcam	ab45270	Citrate	1:500	Yes
Pimonidazole adducts	PIM	Hypoxyprobe, Inc.	HP2-100kit	Citrate	1:100	No
Smooth muscle actin	SMA	Novus Biologicals	NB300-978	Citrate	1:30	Yes
Trop-2	Trop2	R&D Systems	BAF1122	Tryp/Cit	1:1000	Yes

*TSA: tyramide signal amplification

Image manipulation and analysis. Exported TIF files were manipulated in Adobe Photoshop first by applying the curves command to each channel to remove ambient background fluorescence with a linear mapping applied to remaining pixel values. The brightness and contrast of each channel was then optimized for display. All manipulations were applied evenly across an image, and all manipulations were applied identically across a set of images when staining intensity *per se* was an important feature (as opposed to mere visualization of a cell population or structure). Exposure times in these cases were also held constant. For low magnification images of uterine sections, the maximum filter of ImageJ was applied to the green Ly6G-stained channel in order to render PMNs visible. The DAPI (blue) channel was also blurred in some of these cases to improve image quality at low magnification. Since PIM staining visualized hypoxic areas as green and PMNs as red, we inverted these colors in Photoshop for consistency.

For the histomorphometric determination of cross-sectional tumor areas and tumor distributions, Adobe Photoshop was first used to demarcate the E-cad$^+$ epithelium in cross-sections of PRPL uteri or pAKT$^+$ epithelium in longitudinal sections of PL-AdCre uteri, and to further distinguish intact from sloughed epithelium. Sloughed regions were easily identified by eye because they were located within the lumen and had a macerated appearance. For each

sample, ImageJ was then used to determine the cross-sectional areas of the two types of epithelia (intact versus sloughed). For PRPL lesions, this method was also used to determine total, endometrial, myometrial, and luminal cross-sectional areas. SMA co-stain was used to delimit myometrium from endometrium. Derived parameters (percentages) were then averaged across the multiple cross-sections analyzed for each mouse. For PRPL uteri, at least 3 complete and intact cross-sections were analyzed for each 12-week-old mouse; at least 2 complete and intact cross-sections were analyzed for each 4-week-old mouse. For PL-AdCre uteri, total $pAKT^+$ areas (intact and sloughed) were summed from staining of one 5 μm section, which covered the entire length of the uterus.

For the determination of tumor cell BrdU and pH3 labeling indices, the epithelium of each image was first isolated by deleting non-epithelial ($CK8^-$) structures. For the determination of BrdU labeling indices, intraepithelial PMNs were identified (and then deleted) by virtue of their compact, brightly DAPI-positive nuclei, and $BrdU^+$ and total epithelial cells were then hand counted from two 20X images per mouse. At least 1500 cells were scored per mouse. Epithelial nuclear densities were also calculated in relationship to the total epithelial cross-sectional area analyzed, as determined in ImageJ. For the determination of pH3 labeling indices, the number of hand-counted positive cells over 3-5 10X images per mouse was first normalized to the total analyzed epithelial cross-sectional area, again as determined in ImageJ, and this ratio was then converted into a labeling index using the mean epithelial nuclear density for each respective mouse group that was determined as part of the BrdU analysis and shown in Figure S3A.

For the determination of percent $\alpha6^+$ or $\beta4^+$ basolateral epithelial BMZ surface, sections were additionally co-stained with CK8 and DAPI to identify the interface between the epithelium and the stroma, and were analyzed by a standard grid counting method (Weibel, 1969) in Adobe Photoshop. All sections were captured with the same exposure times and manipulated identically in Adobe Photoshop to increase brightness. Data was summated over four 20X random images per uteri from PRPL, PRPL-*Csf3r*$^{-/-}$ and PRPL-*Myd88*$^{-/-}$ mice; data from at least two images per uteri were summated for PL mice.

For determination of PMN density within PIM^- and PIM^+ glands in 4-week PRPL lesions, and within $pAKT^+$ PL-AdCre lesions, the lasso tool and measurement log in Adobe Photoshop were used to delineate and calculate tissue area, respectively. Number of PMNs within a given area was then determined by hand using the count tool. For PRPL lesions, at least 5 20X images from each sample were analyzed, each of which contained from 4-25 distinct glands. Boundaries of uterine glands were easily visualized by increasing the brightness of the green channel (anti-Ly6G). PIM^+ and PIM^- glands were distinguished by eye, and each sample

contained at least 15 total PIM^+ and at least 15 total PIM^- glands. For PL-AdCre uteri, all $pAKT^+$ lesions from a given section were photographed and analyzed. Each sample had at least 9 distinct $pAKT^+$ lesions. Final PMN density for each PRPL and PL-AdCre specimen was determined from summated values for counted PMNs within PIM^+, PIM^- or $pAKT^+$ areas divided by respective summated areas.

Quantitative real-time PCR (qRT-PCR) and whole transcriptome sequencing (RNA-seq). Mouse whole uterine RNA was isolated by homogenization of 1-5 mg tissue in 1 ml Trizol (Life Technologies), followed by chloroform extraction and isopropanol precipitation. RNA from human EC cell lines was isolated using an RNeasy Mini Kit (Qiagen) by following the manufacturer's protocol. cDNA was generated from 1 μg total RNA with an iScript cDNA Synthesis Kit (Bio-Rad), and 3.3 ng cDNA was subjected to qPCR using a cocktail containing 1x EvaGreen dye (Biotium) and 100 nM each of forward and reverse primers (see Supplemental Experimental Tables). Samples were run on an Applied Biosystems StepOnePlus Real-Time PCR System (Life Technologies).

qRT-PCR primers

Gene	Forward Primer	Reverse Primer
MOUSE		
Actb (β-actin)	GCTCTGGCTCCTAGCACCAT	GCCACCGATCCACACAGAGT
Ankrd37	TGGAGACAGGAGCATCAGTG	CCCAAGACATCCTGTTGGTT
Car9 (CAIX)	GCGCTAAGCAGCTCCATACT	CAGCAAAGAGAAGGCCAAAC
Ccl20	CGACTGTTGCCTCTCGTACA	AGGAGGTTCACAGCCCTTTT
Cxcl1	CAAACCGAAGTCATAGCCACA	ACCAGACAGGTGCCATCAG
Cxcl2	CAGGCTACAGGGGCTGTT	CTTCAGGGTCAAGGCAAACT
Cxcl5	GAAAATATTGGGCAGTGACAAAAA	CCGTTCTTTCCACTGCGAG
Cxcr2	GCTCACAAACAGCGTCGTAG	AGGTTCTCTGAGTGGCATGG
Ier3	TCTGGTCCCGAAATTTTCAC	GGACCACTCGAGGGTAGAGC
Il1a	GCTGAAGGAGTTGCCAGAAA	GTGCACCCGACTTTGTTCTT
Il1b	TTTTGACAGTGATGAGAATGACCT	AGCTTCTCCACAGCCACAAT
Il18	ACAACTTTGGCCGACTTCAC	GGGTTCACTGGCACTTTGAT
Il6	CCGGAGAGGAGACTTCACAG	CAGAATTGCCATTGCACAAC
Lgals3	CAACGCAAACAGGATTGTTCTA	TGAATGGTTTGCCACTCTCA
Nampt	CCACCGACTCGTACAAGGTT	ACTTCTTTGGCCTCCTGGAT
Pkm	GTCCGCAGGTTTGATGAGAT	AATCTCAATGCCCAGGTCAC
Plau (uPA)	ACTGCAGGAACCCTGACAAC	TCAGTGAATTCTCCCCCAAC
Ptgs2 (COX-2)	GGCCATGGAGTGGACTTAAA	GGTTCTCAGGGATGTGAGGA
S100a8	GGAAATCACCATGCCCTCTA	TGGCTGTCTTTGTGAGATGC
S100a9	CAGCATAACCACCATCATCG	GTCCTGGTTTGTGTCCAGGT
Slc2a1 (GLUT1)	AAAGAAGAGGGTCGGCAGAT	ACAGCGACACCACAGTGAAG
Tnf	CAGACCCTCACACTCAGATCAT	GTGGGTGAGGAGCACGTAGT
HUMAN		
ACTB (β-actin)	GGACTTCGAGCAAGAGATGG	AGCACTGTGTTGGCGTACAG
CCL20	GCAAGCAACTTGACTGCTG	CGTGTGAAGCCCACAATAAA
IL8	GTGTGAAGGTGCAGTTTTGC	AAATTTGGGGTGGAAAGGTT
PTGS2 (COX-2)	CTGCTCAACACCGGAATTTT	GAGAAGGCTTCCCAGCTTTT
SLC2A1 (GLUT1)	GGGCCAAGAGTGTGCTAAAG	TGCCGACTCTCTTCCTTCAT

For RNA-seq, uterine epithelial cells ($CD45^-EpCAM^+$; see Figure S3D) were sorted on a BC MoFlo XDP (Beckman Coulter) at the NYU School of Medicine Flow Cytometry and Cell Sorting Center. RNA was isolated using an RNeasy Mini Kit. Samples were analyzed on an Illumina HiSeq at the NYU School of Medicine Genome Technology Center. Genes with significantly different expression based on a false discovery rate-adjusted p value ($p_{adj} < 0.05$) in PRPL and PRPL-*Csf3r*$^{-/-}$ tumor cells were clustered into separate groups based on whether expression was higher in PRPL or PRPL-*Csf3r*$^{-/-}$ cells. Gene set enrichment analysis (GSEA) of each group was then performed using the Database for Annotation, Visualization and Integrated Discovery (DAVID; Broad Institute; david.abcc.ncifcrf.gov/tools.jsp). Gene Ontology (GO) Terms with $p < 0.001$ are depicted in Figure 3B. Normalized data for individual genes are depicted in Figures 5E and S6H.

SUPPLEMENTAL REFERENCES

Blaisdell, A., and Erlebacher, A. (2014). Immunofluorescence and Immunohistochemistry. In The Guide to Investigation of Mouse Pregnancy, B. Adamson, A. Croy, A.T. Yamada, F.J. DeMayo, and S. Lee, eds. (Boston: Academic Press), pp. 577-589.

Christopher, M. J., Rao, M., Liu, F., Woloszynek, J. R., and Link, D. C. (2011). Expression of the G-CSF receptor in monocytic cells is sufficient to mediate hematopoietic progenitor mobilization by G-CSF in mice. J Exp Med *208*, 251-260.

Collins, M. K., Tay, C. S., and Erlebacher, A. (2009). Dendritic cell entrapment within the pregnant uterus inhibits immune surveillance of the maternal/fetal interface in mice. J Clin Invest *119*, 2062-2073.

Nowakowski, R. S., Lewin, S. B., and Miller, M. W. (1989). Bromodeoxyuridine immunohistochemical determination of the lengths of the cell cycle and the DNA-synthetic phase for an anatomically defined population. J Neurocytol *18*, 311-318.

Reutershan, J., Morris, M. A., Burcin, T. L., Smith, D. F., Chang, D., Saprito, M. S., and Ley, K. (2006). Critical role of endothelial CXCR2 in LPS-induced neutrophil migration into the lung. J Clin Invest *116*, 695-702.

Weibel, E. R. (1969). Stereological principles for morphometry in electron microscopic cytology. International review of cytology *26*, 235-302.